COMPUTATIONAL AND EXPERIMENTAL INVESTIGATION OF THE CRITICAL ROLE OF TWINNING ON THE PLASTIC DEFORMATION OF HIGH-MANGANESE AUSTENITIC STEELS AND PSEUDOELASTICITY OF NiTi SHAPE MEMORY ALLOYS

by

Berkay Gümüş

A Thesis Submitted to the
Graduate School of Sciences and Engineering
in Partial Fulfillment of the Requirements for
the Degree of

Doctor of Philosophy
in
Mechanical Engineering

Koç University

May 2015

Koç University

Graduate School of Sciences and Engineering

This is to certify that I have examined this copy of a Ph.D. thesis by

Berkay Gümüş

and have found that it is complete and satisfactory in all respects,
and that any and all revisions required by the final
examining committee have been made.

Committee Members:

Demircan Canadinç, Ph.D. (Advisor)

İpek Başdoğan, Ph.D.

Alper Uzun, Ph.D.

Alpay Oral, Ph.D.

Cahit Can Aydıner, Ph.D.

Date: 22.05.2015

ABSTRACT

Several micro-deformation mechanisms are simultaneously activated during the plastic deformation of high-Mn austenitic steels, which does not allow for a clear understanding of the work hardening response of this special class of steels. The major motivation of this thesis was to provide an explanation of the complicated work hardening mechanism in these materials, specifically promoting twinning among other micro-deformation mechanisms with the aid of accelerated loading. With this motivation, numerical analyses were carried out utilizing molecular dynamic simulations with very high strain rates. The initial analyses were focused only on the effect of the grain boundary misorientation angle on the deformation response of pure metallic materials, specifically copper and iron. The results demonstrated the insufficiency of numerical effort as a result of very small samples to be simulated and much more mechanisms take role in the plastic deformation of these materials in addition to grain boundary effects. A comparison between the current simulation results, and the available experimental findings and numerical results at macroscale in the literature has demonstrated that further experimental and numerical analyses should be carried out for clarification. Therefore, the study was extended to a more experimental area where the composition and temperature dependencies of deformation response of high-manganese austenitic steels were investigated under three different loading schemes. First, high-velocity impact loading was utilized in order to examine the microdeformation mechanisms activated. Secondly, the loading velocity was increased via custom compression test setup. Then, an ultra-high velocity loading scenario was applied which was split-Hopkinson tension load. In order to detect the effect of composition, different types of steels, i.e. Hadfield, TWIP, and, XIP steels, with changed alloy contents were tested. On the other hand, for the examination of the effect of temperature, three different temperatures, namely -170 °C, room temperature, and 200 °C were selected as testing temperatures. The promotion of twinning over other mechanisms due

to applied accelerated loading was investigated thoroughly with numerous methods which are scanning electron microscopy, transmission electron microscopy, confocal laser scanning microscopy, and, optical microscopy. In addition, a thermal perspective was adopted for impact tests as *in situ* thermographical analyses were conducted to detect the temperature change related to the hit of impact hammer. Various mechanisms such as slip, formation of more than one twin variant, nano-twins inside primary twins and voids were activated in Hadfield steel, while the deformation was twin-dominated in TWIP steel at all temperatures, which stems from the increase in stacking fault energy (SFE) due to the higher Mn content. Moreover, nano-twin formation within one primary twin system was observed for TWIP steel at subzero temperatures. The XIP steel with the highest SFE, on the other hand, deformed mostly by slip at elevated temperatures, although twins and nano-twins dominated the microstructure as the temperature decreased to room temperature, and then to -170 °C, respectively. The current set of results lay out the roles of temperature, deformation velocity and alloy content on the microstructure evolution of high-Mn steels, which altogether can be tailored to improve the work hardening capacity of this class of materials.

In addition to high-manganese austenitic steels, another class of materials, i.e. nickel-titanium (NiTi) shape memory alloys, was investigated due to the significant role of twinning on material properties. Specifically, NiTi alloys have three properties, namely one- and two-way shape memory effects and pseudoelasticity, which all take place by solid to solid phase diffusionless transformation via twinning and detwinning upon the application of either load or temperature change. Among these three, the pseudoelasticity was taken into consideration in the current work. First, the fatigue performance of micro-scale pseudoelastic NiTi wires was investigated under cyclic bending loading. The current findings demonstrated that the change in the scale from macroscopic to microscopic promotes the formation of the B19' phase and significantly hinders stabilization of the R-phase. Second, a rather application-

based study was also conducted on NiTi orthodontic archwires. The NiTi orthodontic wires were examined in terms of their biocompatibility via mimicking the actual contact state of wires around brackets in intraoral environment. These wire-bracket contacts made the simulation of mechanical loading at the wires possible during *ex situ* experiments. An undeformed wire and another set which was bound to brackets on a plaster dental model were immersed into artificial saliva solution for a period of 31 days. Post-immersion electron optical analyses were carried out on the wires, while inductively-coupled plasma mass spectroscopy was conducted on the solutions. The carbon-rich product formation was detected on both undeformed and bound wires after immersion. This formation was observed to be randomly distributed on the undeformed wire, while it was localized on certain locations with equivalent intervals on the bound wires. This localization of corrosion products was then attributed to the preferential formation at the wire-bracket contact regions due to higher surface energy attained and micro-scale cracks formed at these regions after optical microscopy analyses. Furthermore, the limited amount of Ni or Ti ion release into the solutions was attributed to the suggested blocking of micro-cracks with these corrosion products. The current set of results revealed the importance of the simulation of chemical and mechanical conditions of the intraoral environment simultaneously for a more reliable and realistic investigation of the biocompatibility of NiTi orthodontic wires.

ÖZET

Yüksek manganlı östenitik çeliklerin plastik deformasyonu sırasında birlikte etkinleşen mikro mekanizmalar nedeniyle, bu özel sınıf çeliklerin pekleşme davranışları açıkça anlaşılamamaktadır. Bu tez çalışmasının ana motivasyonu, hızlandırılmış yüklemelerle tüm mekanizmalar içinden ikizlenmeyi tetikleyerek, bu malzemelerin karmaşık pekleşme davranışına bir açıklama getirmektir. Bu motivasyonla, yüksek gerinim hızları kullanılan moleküler dinamik simülasyonları ile sayısal analizler yapılmıştır. Başlangıç analizlerinde yalnızca tanecik sınırı düzensizlik açısının özellikle bakır ve demir olmak üzere saf metalik malzemelerin deformasyon tepkisine etkisi incelenmiştir. Sonuçların ortaya koyduğu üzere, bu malzemelerin plastik deformasyonu sırasında tanecik sınırı etkilerine ek olarak pek çok mekanizmanın etkimesi ve simülasyonu yapılan numunelerin çok küçük olması sebebiyle sayısal çabanın eksik kaldığı gözlenmiştir. Bu simülasyon sonuçları ile önceden rapor edilen deneysel bulgular ve makro ölçekteki sayısal sonuçlar kıyaslandığında, bu malzemelerin deformasyon tepkisinin aydınlatılması için daha fazla deneysel ve sayısal analize gerek olduğu anlaşılmıştır. Bu nedenle, çalışma bileşim ve sıcaklık etkisinin yüksek manganlı östenitik çeliklerin deformasyon tepkisine etkisinin üç farklı yükleme planı altında incelendiği daha fazla deneysel bir alana genişletilmiştir. İlk olarak, yüksek hızlı çarpma deneyleri ile etkinleşen mikro deformasyon mekanizmaları incelenmiştir. İkinci olarak, isteğe uyarlanmış bir basma deney düzeneği ile yükleme hızı artırılmıştır. Daha sonra, split-Hopkinson basınç bar yöntemiyle çok yüksek hızlı yükleme senaryosu uygulanmıştır. Alaşım bileşiminin etkisini saptamak için, bileşimleri farklı olan Hadfield, TWIP ve XIP türü çeliklerde deneyler yapılmıştır. Diğer yandan, sıcaklığın etkisini incelemek için -170 °C, oda sıcaklığı ve 200°C olmak üzere üç sıcaklık seçilmiştir. Taramalı elektron mikroskopisi, geçirimli elektron mikroskopisi, eşodaklı lazerli tarama mikroskobisi ve optik mikroskopi olmak üzere bir çok yöntemle, yüksek hızlı yüklemeler ile ikizlenmenin diğer mekanizmalara oranla tetiklenmesi

kapsamlı olarak incelenmiştir. Buna ek olarak, çarpma deneyleri sırasında yerinde termografik analizler yürütülerek çekicin çarpmasına bağlı olan sıcaklık değişimleri incelenmiş, bir termal bakış açısı benimsenmiştir. Hadfield çeliğinde; sekme, birden fazla ikizlenme değişkesi, birincil ikizlenmeler içinde nano ölçekli ikizlenmeler ve boşluklar olmak üzere bir çok mekanizma etkinleşirken, daha yüksek mangan içeriği sebebiyle daha yüksek istif bozukluğu erkine sahip olan TWIP çeliğinin deformasyon tepkisinde baskın mekanizma bütün sıcaklık değerlerinde ikizlenme olarak saptanmıştır. Bununla birlikte sıfıraltı sıcaklıklarda, TWIP çeliğinde birincil ikizlenmeler içerisinde nano ölçekli ikizlenmeler oluştuğu belirlenmiştir. Diğer yandan, en yüksek istif bozukluğu erkine sahip olan XIP çeliğinin, yüksek sıcaklıklarda çoklukla sekme mekanizmasıyla deforme olurken sıcaklık oda sıcaklığına ve sonra -170 °C'ye düşürüldüğünde sırasıyla, ikizlenme ve nano ölçekli ikizlenme mekanizmalarıyla baskın olarak deforme olduğu gözlenmiştir. Bu sonuçlar, yüksek manganlı çeliklerin pekleşme kapasitesinin geliştirilmesi için değiştirilebilecek; sıcaklık, yükleme hızı ve alaşım bileşim etkilerinin, yüksek manganlı çeliklerin mikroyapı yayılımı üzerindeki rolünü ortaya koymuştur.

Yüksek manganlı östenitik çeliklere ek olarak, bir başka malzeme sınıfı; nikel-titanyum (NiTi) şekil hafıza alaşımları da ikizlemenin malzeme özellikleri üzerindeki önemli etkisi sebebiyle incelenmiştir. NiTi alaşımları, yük ve ya sıcaklık değişimlerine bağlı olarak gözlenen ve yayınımsız katı hal faz değişimlerinden kaynaklanan üç özelliğe sahiptir ve bunlar, tek ve çift yönlü şekil hafıza etkisi ve süperelastisitedir. Bu çalışmada bu üç özellikten süperelastisite dikkate alınmıştır. İlk olarak mikro ölçekteki süperelastik NiTi tellerin çevrimsel eğme yükü altında yorulma performansı incelenmiştir. Bulgular makro ölçekten mikro ölçeğe geçerken B19' fazı oluşumunun arttığını ve R-fazı dengelileşmesinin önemli ölçüde engellendiğini göstermiştir. İkinci olarak, daha fazla uygulama temelli bir çalışma, NiTi ortodontik ark telleri üzerinde yürütülmüştür. Ağıziçi ortamda NiTi ark tellerinin

braketler ile oluşturduğu gerçek değme durumu taklit edilerek bu tellerin biyouyumlulukları incelenmiştir. Bu tel-braket değme durumu tel üzerindeki mekanik yüklerin ortamdışı simülasyonunu mümkün kılmaktadır. Bir adet deforme edilmemiş ve bir adet ağız modeline sabitlenmiş braketlere bağlanmış olmak üzere teller 31 gün boyunca yapay ağızıçi sıvısına daldırılmıştır. Daldırma sonrası teller üzerinde elektron optik analizler yürütülürken sıvılar üzerinde etkileşik çiftlenmiş plazma kütle spektroskopisi analizi yapılmıştır. Deney sonrası, hem deforme edilmemiş hem de daldırılmış tel üzerinde karbonca zengin ürün oluşumu belirlenmiştir. Bu oluşum deforme edilmemiş tel üzerinde rastgele dağılmış durumdayken, diğer tel üzerinde belli aralıklarla yoğunlaşmış olarak gözlenmiştir. Optik mikroskopi analizlerinden sonra, korozyon ürünlerinin bu yoğunlaşması, tel-braket değme noktalarındaki yüksek yüzey enerjisi ve mikro ölçekli çatlaklar sebebiyle, bu noktalardaki tercihli oluşumlara bağlanmıştır. Ek olarak, sıvılar içerisinde sınırlı miktarda Ni ve ya Ti iyon salınımı da bu mikro ölçekli çatlakların korozyon ürünlerinin oluşumuyla kapanmasına bağlanmıştır. Bu sonuçlar, NiTi ortodontik ark tellerinin biyouyumluluk araştırmalarında, ağızıçi ortamının hem kimyasal hem de mekanik koşullarının aynı anda tam olarak simülasyonunun daha güvenilir ve gerçekçi incelemeler için gerekliliğini ortaya koymuştur.

ACKNOWLEDGEMENTS

I would like to thank Dr. Demircan Canadinç not only for welcoming me to work in this very delightful group and for his guidance throughout all these three years, but also for his heartfelt advices and understanding. Alongside these, I am grateful to him for giving me the chance of working at one of the largest facilities in Germany, IW in Hannover. I would like to thank Dr. Gregory Gerstein and Andrej Dalinger, and all other staff at IW for all their help and time during experiments. I would also like to thank Prof. Hans J. Maier for his generous invitation to IW. I am and will eternally be thankful to my family for their support and trust in me and my decisions all the time. Not different from them, I am grateful to my dear Nazik for all her assistance and contribution to my life. Lastly, I owe a lot to my friends, S. Mine Toker, Burak Bal, Benay Uzer, Cemre Özmenci, Morad Mirzajanzadeh, and Orkun Önal for being with and helping me during hard times. I want to thank GSSE and CE staff at Koç University for the great working environment and their support. This thesis was supported in part by TÜBA-GEBİP and Roketsan Missiles Industries Inc..

Dedicated to my family…

Table of Contents

List of Tables

List of Figures

PART 1: A COMPARATIVE APPROACH ON THE INVESTIGATION OF THE MECHANICAL RESPONSE OF HIGH-MANGANESE AUSTENITIC STEELS

1.1 INTRODUCTION

1.1.1 Motivation and Background

Excellent combination of high strength, significant ductility, high toughness, large strain hardening capacity and impressive wear resistance have made high-manganese (Mn) austenitic steels the material of choice for various applications in automotive, defense, railroad and mining industries for decades [1]. The remarkable combination of the aforementioned mechanical properties stems from the complicated micro-deformation mechanisms, such that usually more than one is effective and the different mechanisms interact with each other [2–37]. This complexity of the micro-deformation mechanisms in high-Mn austenitic steels has been the subject of research in many studies aiming to understand the exact cause of the exhibited rapid strain hardening to tailor the properties of this class of materials for further improving their performance in service [1,11–15,17,21,23,25–28,31–34,37–54].

One of the major conclusions drawn from the large volume of previous work on high-Mn austenitic steels is that both slip and mechanical twinning become simultaneously activated for most of the deformation, such that they both separately contribute to the overall strain hardening and further interact with each other to enhance the strain hardening [2–13,17,25–28,31–34,37–41,43–48,55–60]. Specifically, the coexistence of slip and twinning provides a means of dissipating the added energy imposed upon by deformation, leading to the out-of-the-ordinary ductility exhibited by these steels [2,12–17,21,25,32,34,38–41,44,47,48,51]. In addition, twin boundaries forming throughout the deformation constitute

effective barriers against dislocation glide, leading to the rapid strain hardening with increasing strain, which is typical of high-Mn austenitic steels [3–5,7–10,16,17,32,37,38,41,57–63]. Furthermore, formation of new twins becomes easier with ongoing deformation since dislocation pile ups and existing twin boundaries constitute ideal nucleation sites for new twins [64]. Moreover, secondary or tertiary twin systems can also be activated along with primary twins during deformation, which enhances the strain hardening capacity of high-Mn steels as they create stair-like structures against dislocation motion [26,65]. These stair-like structures act as effective obstacles against dislocation motion, leading to and enhanced overall strain hardening upon plastic deformation. This complexity is further increased by other microstructural features, such as grain boundaries, voids or interstitials, since they also interact with and influence the activities of slip dislocations and twins [2,4–7,10–17,20,21,25–27,32–34,37–39,41,43,45,55–57,60–63]. The dominant mechanism and the possible interactions are dictated by multiple parameters, such as temperature, strain rate and chemical composition [11–16,21,32,33,47,60,63,66].

Among these parameters, the chemical composition is especially decisive since the stacking fault energy (SFE) is dictated by both temperature, and the contents of Mn, carbon (C) and other alloying elements, such as aluminum (Al) or silicon (Si) [2,4,16,17,21,41,61]. Specifically, the SFE increases concomitant with temperature [11,12] owing to the increase in Gibbs free energy change needed for deformation [11]. However, the role of chemical composition depends on the particular contents of alloying elements: for instance, while the addition of Al increases the SFE, alloying with Si decreases it [13,23,67]. The SFE energy level dictates the major deformation mechanism observed in this class of steels, such that either transformation-induced plasticity (TRIP), twinning-induced plasticity (TWIP) or dislocation glide facilitate the plastic deformation. In particular, the TRIP effect prevails, i.e. an austenite-to-ε-martensite transformation takes place, below an SFE level of 18-20 mJ/m^2

whereas extensive mechanical twinning takes place throughout the microstructure in the SFE range of 12-35 mJ/m^2 [15]. At these relatively lower SFE levels it is easier to overcome the energy barriers to accommodate abrupt changes in the lattice by martensitic transformation (TRIP) or mechanical twinning (TWIP), while higher SFE levels than 35 mJ/m^2 promote dislocation slip [15,16].

In addition to SFE, dynamic strain aging (DSA) should also be considered when investigating the deformation behavior of high-Mn austenitic steels [18,42]. During straining, due to enhanced diffusion, the soluble C atoms of C-Mn couples placed at dislocation cores are repositioned to another interstitial site. This repositioning makes also the C atoms mobile within the microstructure, which increases their capability of pinning mobile dislocations, leading to DSA. A large number of studies focusing on the role of DSA to the overall hardening of high-Mn steels [2,6,19–23,62,68] have shown its contribution through different mechanisms, such as the effects of chemical composition, which dictates the number of C-Mn couples [2,19–23,68], or the carbide formation during deformation [6]. For example, Al addition was shown to decrease the C activity and diffusivity, hence, weaken the role of DSA [2,21]. Moreover, addition of nitrogen (N) was found to increase the critical strain for DSA, which restricts the role of DSA at the earlier stages of deformation in high-Mn steels [22]. On the other hand, although carbide formation promoted by alloying elements within the material results in the absence of C atoms and decrease in the strain hardening capacity through pinning the dislocations, i.e. DSA, this is not the case for high-Mn steels due to the high contents of C and Mn in the matrix [6]. Another significant effect of DSA reveals itself in the negative strain rate sensitivity (NSRS) in high-Mn austenitic steels [62,69], such that DSA leads to softening of the material: in general, dislocation density increases concomitant with strain rate, further enhancing the hardening of the material due to forest hardening. In this specific class of steels, however; within a certain strain rate range, the softening effect of the

DSA overcomes the hardening due to forest dislocations despite the increasing strain rate, leading to the softening of the material and NSRS. Upon further increase of the strain rate beyond the NSRS range, forest hardening dictates the deformation response, and the general trend of hardening concomitant with increased strain rates is resumed [62]. In the current study, in order to eliminate the softening effect of DSA, high-velocity testing scenarios were utilized, featuring strain rates beyond the NSRS range.

A large volume of previous investigations exist on the roles of phase transformation, twinning, slip, DSA, and complex interactions between all these micro-deformation mechanisms on the rapid strain hardening behavior exhibited by high-Mn austenitic steels [17,31–36,44,70]. However, an investigation focusing on the contribution of nano-twin formation within the pre-existing twins to the overall strain hardening in this class of materials is not available yet. These secondary and tertiary nano-scale twins may indeed further improve the strain hardening capacity by dissipating more energy that cannot be dissipated by dislocation slip or primary twinning [36].

1.1.2 Methods and Preliminary Work

In this part of the thesis, a numerical approach was developed in order to understand the mechanical response of high-Mn austenitic steels (Chapter 1.2). For this purpose, to simplify the simulations, copper (Cu) and iron (Fe) were investigated utilizing molecular dynamics (MD) simulations, where Cu and Fe samples composed of two individual grains with a certain grain boundary misorientation angles (GBMA) were analyzed to detect the effect of GBMA on the deformation response, and in particular, work hardening. A very high strain rate was applied in MD simulations, namely 10^9 s^{-1}, in order to avoid significantly longer computational periods required for slower rates of deformation. The preliminary results revealed that an increase in GBMA results in a random increasing and decreasing

effect on the strength of the Cu and Fe for different angle values. Overall, these results indicated the effect of individual grain orientation on the strength of the material since the active deformation systems, hence the deformation response of the material, are strongly related to the orientation of the grains with respect to the applied strain. Moreover, having only two grains in the sample might has an effect on these randomized results. Based on these conclusions, simulations were extended to samples with seven grains with changing angles in between. When the results were compared with experimental results available in the literature about the effect of GBMA on the mechanical behavior of metallic materials, the study was extended to a more experimental pathway for the clarification of the complicated deformation response of metallic materials, and in particular, high-Mn austenitic steels.

Following the numerical analyses, a thorough microstructural investigation was carried out in order to determine the aspects of the superior strain hardening capability of high-Mn steels with different chemical compositions. The experimental conditions, such as test temperature and velocity, and the alloy composition, play a significant role for the observation the dictating micro-mechanisms and the resulting deformation behavior. For this purpose, first, Charpy impact tests (Chapter 1.3) were conducted on two types of high-Mn steels, namely TWIP and XIP (also commercially named as X-IP™ 1000 (provided by Arcelor Mittal) steels. Secondly, high-velocity compression tests (Chapter 1.4) were carried out on these two steels along with well-known Hadfield steel in order to investigate the micro-scale deformation behavior under more accelerated loading scheme, i.e. 3-8 m/s. Then, the speed of deformation was further increased utilizing a split-Hopkinson bar (SHB) tensile test setup (Chapter 1.5). The basic idea for the application of deformation with higher velocities than conventional tests was to trigger twinning over all micro-mechanisms activated in plasticity of high-Mn steels to simplify the determination of complex mechanical response of the high-Mn steels. In addition to change in deformation velocities, all the experiments were

carried out at three temperatures, i.e. -170 °C, room temperature (RT), and 200 °C. The reason for changing the test temperature was the effect of temperature on the deformation aspects such as the twin volume fraction, twin thickness and glide dislocation density. The SFE of Hadfield, TWIP, and XIP steels at room temperature are about 21 mJ/m^2, 19 mJ/m^2, 26 mJ/m^2, respectively, for the steels with similar chemical composition [53,71]. The microstructure and deformation mechanisms of the as-is and deformed materials were investigated by optical microscopy, stereographic microscopy, scanning electron microscopy (SEM) and transmission electron microscopy (TEM). In addition, for high-velocity compression tests, post-deformation confocal laser scanning microscopy (CLSM) analyses were carried out.

1.2 INVESTIGATION OF THE EFFECT OF GRAIN BOUNDARY MISORIENTATION ANGLE ON THE WORK HARDENING BEHAVIOR OF METALLIC MATERIALS

1.2.1 Theory and calculation

In order to simulate the deformation response of copper (Cu) and iron (Fe), molecular dynamics (MD) simulations were carried out utilizing Large-scale Atomic Molecular Massively Parallel Simulator (LAMMPS) script. The theory of MD simulations is based on the integration of Newton's equations for each of the atoms in the structure of a material, which are assumed as point masses to compute the motion of these atoms in the space [72]. These equations are as follows for an atom i with a neighbor atom j [72]:

$$m_i \frac{d\vec{v_i}}{dt} = \sum_j F\left(\vec{r_i}, \vec{r_j}\right) + \ldots\ldots\ldots \quad (1)$$

$$\frac{d\vec{r_i}}{dt} = \vec{v_i} \quad (2)$$

where m_i, $\vec{r_i}$, and, $\vec{v_i}$ are the mass, and position and velocity vectors of atom i, respectively. In addition, F is the force function corresponding to the pairwise interaction between atoms i and j. The Eq. 1 continues with the higher order interactions, i.e. three-body and many-body interactions. In LAMMPS, these long-range interactions are neglected as the force integration is limited within a cut-off distance from atom i [72]. Through these calculations, a wide range of information can be gathered, such as the thermal or structural changes during the simulation [72]. The atomistic basis of MD simulations reveals purely physical results based on potential energy calculations. However, since the length scales are at Angstrom levels, i.e. 10^{-10} m, and time scales are at femtoseconds, i.e. 10^{-15} s, the simulation of a sub-micron structure, i.e. 10^{-6} m, for picoseconds, i.e. 10^{-12}, requires a vast amount of computational time.

The high computational cost of classical MD simulations has opened a venue on decreasing the simulation time by parallelizing the procedure, which led to several algorithms, including LAMMPS. Specifically, for parallel computations in LAMMPS, spatial-decomposition method is utilized [72]. Through this method, the physical domain is divided into three dimensional boxes for each processor, and the force calculations are carried out only for assigned box by the corresponding processor. At each time step, based on force calculation, the position and the velocities for atoms are updated. Since atoms move in the physical domain, they are reassigned to a new processor at every time step [72]. For the physics-based computation of atomic forces, interatomic potential energy is utilized, which is available in the literature for some materials and material pairs for specific alloys.

In the current simulations, octahedral specimens were created with different number of grains of certain orientations, corresponding to the varying grain boundary misorientation angles (GBMA). The interatomic potentials were then implemented for Cu [73] and Fe [74] individually. After the formation of the simulation box (Figure 1.2.1), the energy of the system was minimized by iteratively changing the atom coordinates while the iteration tolerance was defined as 10^{-15} both for energy and force. Following the first energy minimization step, a secondary minimization was conducted together with stress relaxation along the deformation axis. At the end, tensile deformation was applied with a specified strain rate through which the strain and stress data were collected for further analyses.

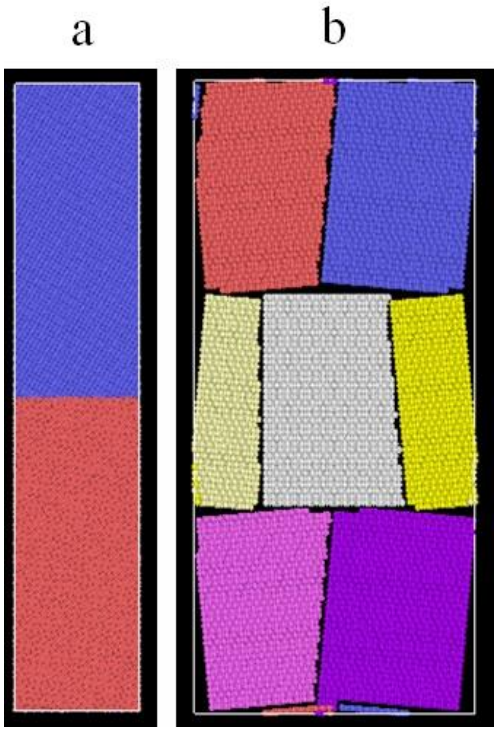

Figure 1.2.1 Simulation boxes for (a) two grains formed with certain orientations (b) seven grains formed by the rotation other than the one in the middle

1.2.2 Results and discussion

For the investigation of the effect of GBMA, two neighbor grains created between which the angle changing systematically from 2.5 to 67.5 degrees (Figure 1.2.1(a)). The tensile deformation simulations were carried out on both Cu and Fe of which the results were demonstrated in Figure 1.2.2 and 1.2.3, respectively. The stress values in these graphs are significantly higher than the values in conventional experiments, which is due to theoretical basis of the MD simulations where atomistic scale modeling carried out on a very small specimen with almost no defects within the microstructure. As opposed to the macroscopic strengthening trend with the increase in GBMA, the behaviors of certain angles were changed especially for the initial stages of deformation where only limited amount of grain rotation takes place (Figures 1.2.1 and 1.2.2). On the other hand, when deformation proceeds, grains

rotate such that the angle between them is not the same as the angle defined initially. Hence, only the initial stages of deformation were taken into consideration during the investigation of hardening behavior. Upon this consideration, the stress-strain lines for simulated angles behave randomly when the angle was increasing.

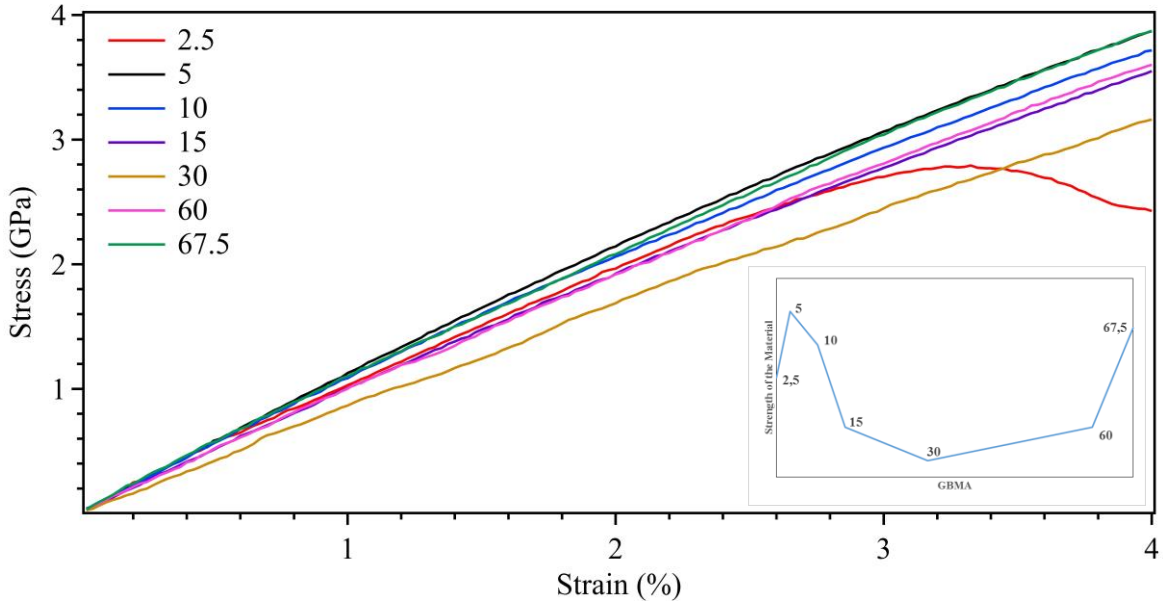

Figure 1.2.2 Stress-strain graph of Cu for changing GBMA (values in legend are in degrees and the inset is showing the relative strength of material vs. GBMA)

The increasing and decreasing trend in the tensile strength of Cu was evident by the increase in GBMA (Figure 1.2.2). However, it should always as the strengthening of the material due to the increased disorder at grain boundaries with higher angles. The higher angles require higher energies in order for dislocations to overcome the barrier, i.e. grain boundary in this case. However, there were some exceptions for GBMA of 15, 30, and 60 degrees where the strength of the material was lower than that of the lower angles for each case.

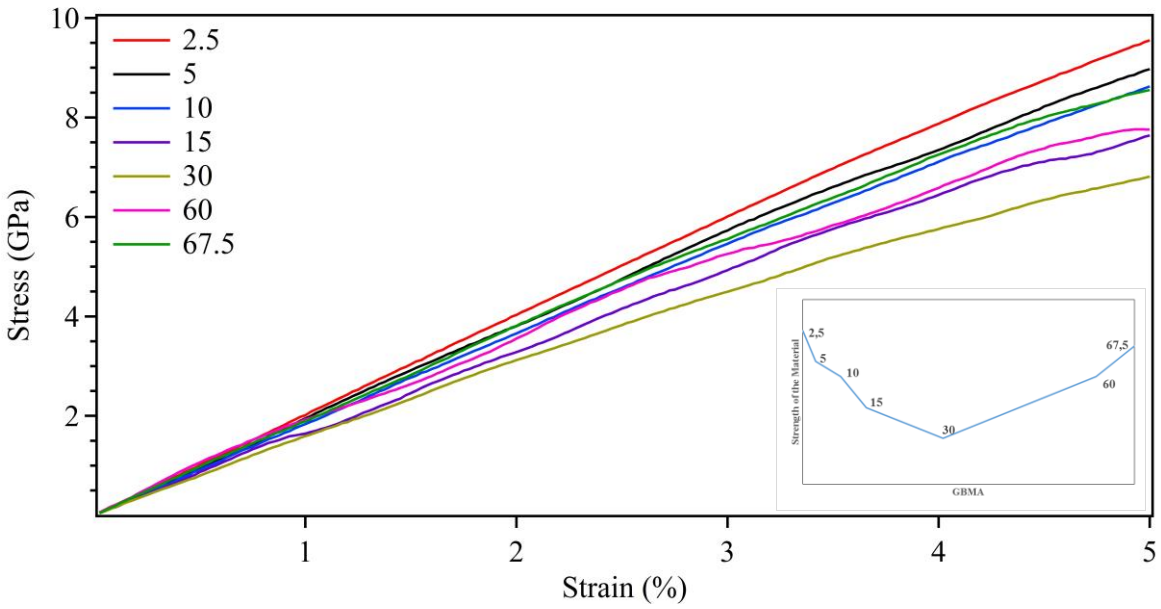

Figure 1.2.3 Stress-strain graph for Fe for changing GBMA (values in legend are in degrees and the inset is showing the relative strength of material vs. GBMA)

On the contrary to Cu, there was no exact trend of the hardening behavior of iron for the same orientations, i.e. the GBMA values between 2.5 to 67.5 degrees. Specifically, the material was hardened by the change in GBMA from 30 to 60 degrees, while it was softened when GBMA was changed from 2.5 to 5 degrees. This irregular response was suggested as the result of the relative orientation of grains with respect to deformation direction. Since the activated deformation systems in the lattice are dependent on the direction on which the deformation is applied, the hardening behavior due to change in GBMA may differ. Therefore, the hardening behavior was further investigated by changing this relative orientation.

In order to have a better understanding on the effect of GBMA on the hardening behavior of Cu and Fe, seven different grains were formed in the simulation box between which the angles were changing between 2.5 to 15 degrees (Figure 1.2.1(b)). For this purpose, one grain in the middle was fixed to the orientation of [111] on the loading axis which is

known as one of the slip direction to be activated first since it is one of the most densely packed directions. The other surrounding grains, on the other hand, rotated before the deformation step such as the grain boundaries in between have angle values ranging between 2.5-5, 5-10 and 10-20 degrees. Through this approach, the relative orientation of deformation with respect to lattice orientation was changed. The results are illustrated in Figure 1.2.4 and 1.2.5 for Cu and Fe, respectively.

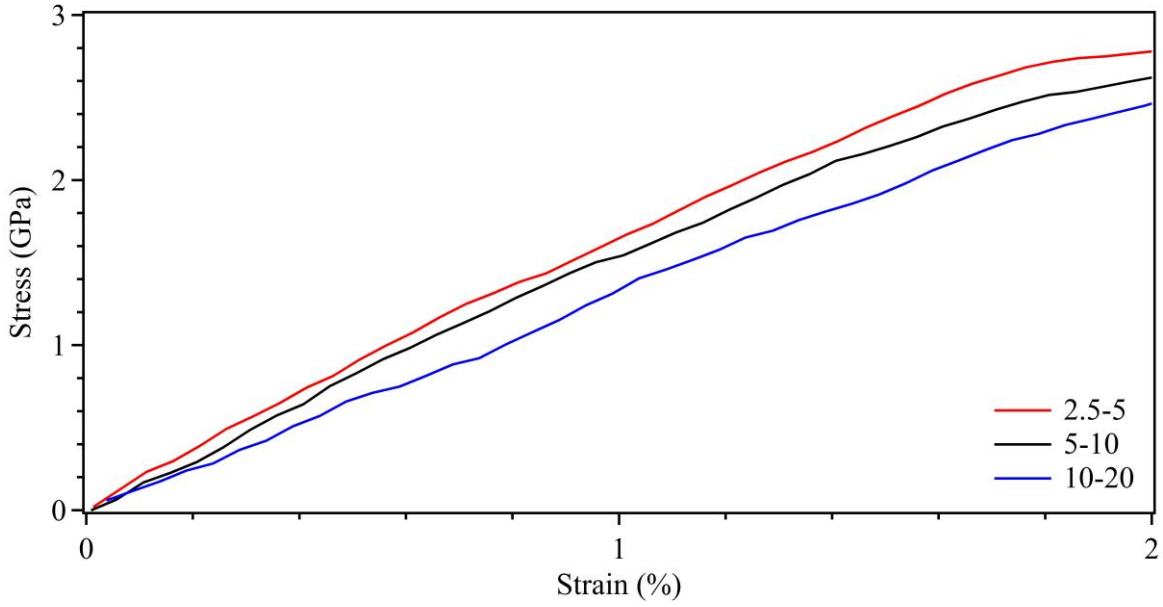

Figure 1.2.4 Stress-strain graph for Cu with 7 grains for changing GBMA (values in legend are in degrees).

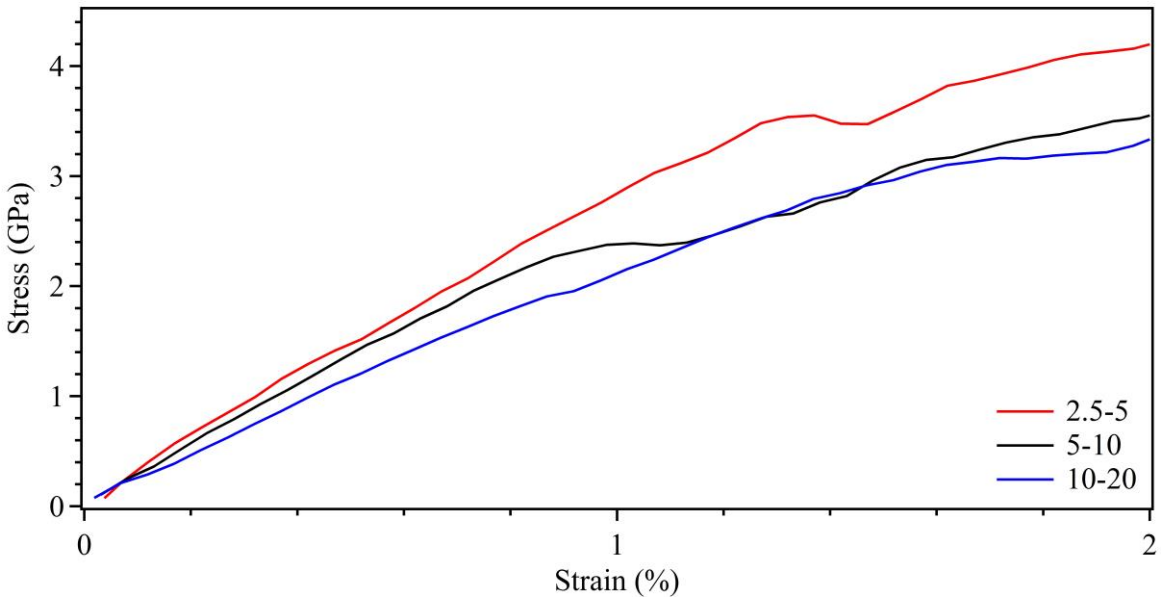

Figure 1.2.5 Stress-strain graph for Fe with 7 grains for changing GBMA (values in legend are in degrees).

The softening response of Cu under tension was clearly demonstrated for the simulations conducted on the sample with increased number of grains, i.e. seven grains. In addition to Cu, same response was observed for Fe sample indicating the lack of numerical approach to the investigation of the mechanical behavior of metallic materials.

1.2.3 Summary

The inadequacy of numerical investigation was put forward after MD simulations with different due to less number of grains introduced into the system and the absence of other microconstituents of the hardening of these materials. Hence, a deeper experimental effort was employed in the forthcoming chapters in order to detect all mechanisms take role in the hardening behavior of high-Mn austenitic steels which must be incorporated into the numerical analyses to get correct results.

1.3 ON THE MICRO-DEFORMATION MECHANISMS ACTIVE IN HIGH-MANGANESE AUSTENITIC STEELS UNDER IMPACT LOADING [75]

1.3.1 Experimental Details

For the investigation of the micro-deformation mechanisms facilitating the plastic deformation of high-Mn austenitic steels, a wide range of experiments were carried out. In the first part of experimental work, two types of high-manganese austenitic steels, namely a TWIP steel and an XIP steel, were utilized in the impact experiments of which the chemical compositions are given in Table 1.3.1 Following the standard metallographic sample preparation steps, microhardness values in HV0.1 scale of all samples around the notch were measured using a micro-hardness tester. Line measurements were taken around the critical region for impact deformation, i.e. the sides of the notch. The initial average Vickers hardness of TWIP and XIP steels were observed as 280 and 330 HV, respectively. Moreover, the hardness values were nearly uniform around the notch proving the presence of nearly uniform initial microstructure of the samples.

Table 1.3.1 Chemical compositions of TWIP and XIP steels (wt. %).

Steel	C	Si	Mn	Ni	Cr	V	Co	Ti	Fe
TWIP	0.628	2.601	14.843	0.065	0.043	0.023	0.012	0.006	Balance
XIP	0.600	0.190	20.990	0.018	0.118	0.129	0.011	0.004	Balance

For the impact tests, Charpy-V shaped TWIP samples with dimensions of 55 mm × 10 mm × 2 mm, and XIP samples with dimensions of 50 mm ×10 mm ×2 mm were prepared

utilizing electro-discharge machining[1]. All impact samples featured a 45° notch with a radius of 0.25 mm and a depth of 2 mm. The experiments were carried out at three different temperatures, namely -170 °C, room temperature (RT) and 200 °C. The samples were cooled down to -170 °C with liquid nitrogen while heated up with furnace. The measured impact energies of XIP and TWIP steels at each temperature are plotted in Figure 1.3.1 which demonstrates that the ductile-to-brittle transition temperatures for both steels were below RT. Since the ductile-to-brittle transition is within the range of impact experiments, both the low temperature brittle response and the high temperature ductile behavior, as well as the transition range can be observed. In addition, from a thermal perspective, the changes in the temperature of the sample due to impact loading until fracture were detected by a thermal camera operated in-situ. SEM and TEM observations were performed in order to obtain information about the TWIP effect and the activated micro-mechanisms under impact loading.

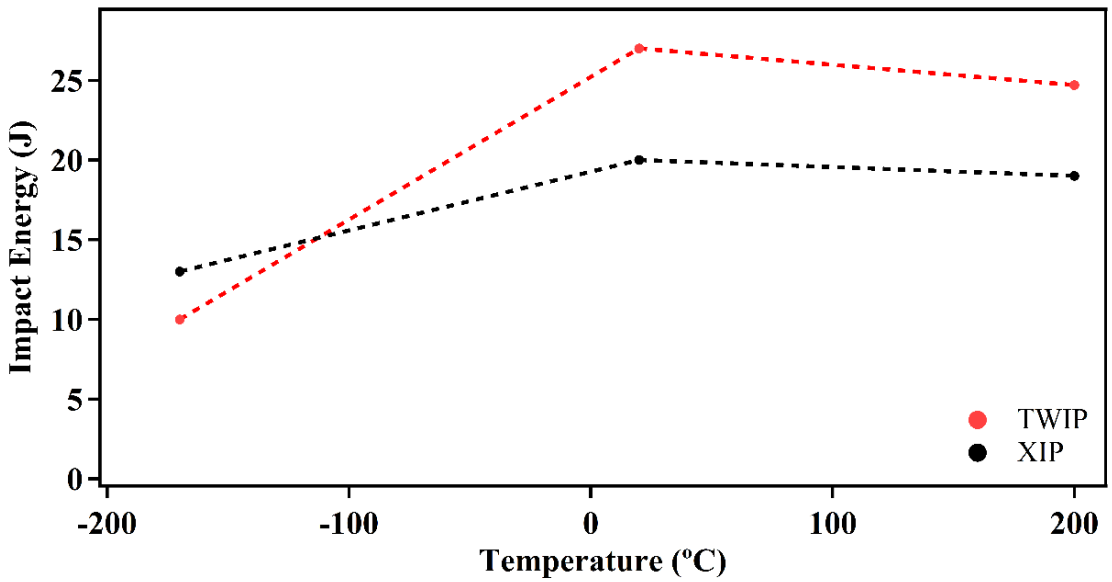

Figure 1.3.1 Impact energy vs. temperature plot for the XIP and TWIP steels.

[1] This slight difference in sample dimensions stems from the geometry of the XIP steel initially available.

1.3.2 Results and Discussion

1.3.2.1 Microstructural investigation

The activated micro-mechanisms upon impact loading in TWIP and XIP steels at all three temperature are summarized in Table 1.3.2.

Table 1.3.2 Deformation mechanisms observed at all temperatures for the TWIP and XIP steels.

	200 °C	**RT**	**-170 °C**
TWIP	2 T, S, V	TT, S, V	TT, S, V
XIP	S	2 T, S, V	TT, S
S: slip T: twin TT: twin-inside-twin V: void formation			

The results indicated that slip, twinning and void formation mechanisms coexist in the deformation response of TWIP steel which has the lower Mn content at 200 °C as shown in Figure 1.3.2. Specifically, in Figure 1.3.2(a), the two-varianted twinning scheme was shown together with the dislocations throughout the microstructure. Moreover, the voids formed preferentially at grain boundaries were illustrated in Figure 1.3.2(b) for the sample deformed at 200 °C. activated two twin variants agree well with a previous study where high velocity ballistic impact tests were conducted at RT [76]. The ballistic penetration present in that study resulted in a jump in the temperature of the sample which causes deformation to take place at high-temperatures locally [76]. The mechanisms observed were similar to the ones in the current work which are mainly twinning with two variants and dense dislocations interacting with these twins [76]. On the contrary to two twin variants activated at elevated temperatures, the secondary nanoscale twin formation inside preformed twins was observed following the decrease in the temperature down to RT (Figure 1.3.3(a)), and then to -170 °C (Figure 1.3.3

(b)). These nanotwins in TWIP steel deformed at RT was not demonstrated in studies where conventional uniaxial tension [33] and high-pressure torsion experiments [29] were conducted on materials with closer chemical composition. In tension experiments, a secondary twin system was observed in addition to the primary twins [33]. For the high-pressure torsion experiments, secondary and tertiary twin systems rather than nanoscale twins were shown to be formed when two and three torsional cycles were applied, respectively [29]. Not only the twinning scheme was changed upon temperature decrease but also the dislocation activity was decreased when temperature is lowered down to RT (Figure 1.3.3(a)) then to -170 °C (Figure 1.3.3(b)) such that a low density of dislocations and rare dislocation-twin interactions were observed.

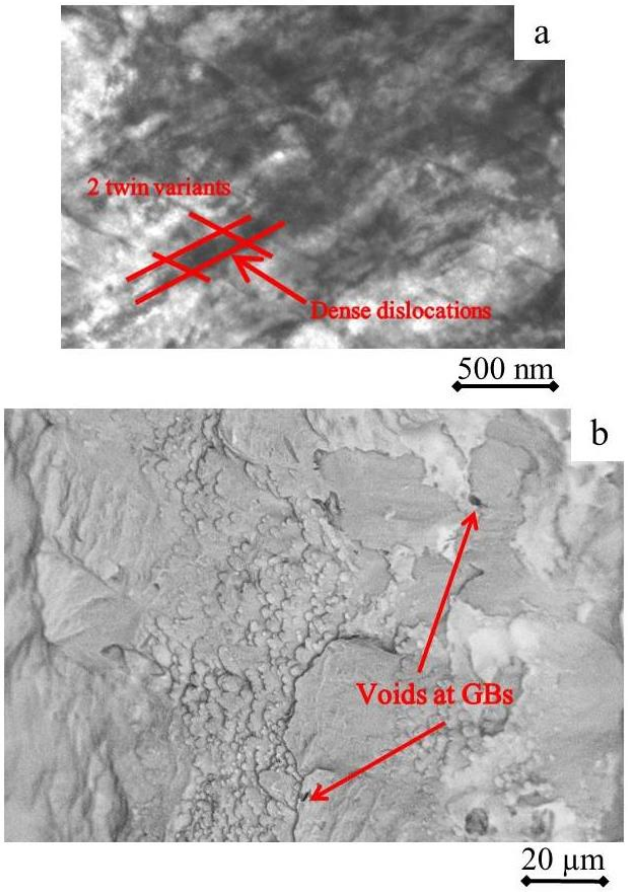

Figure 1.3.2 (a) The two twin variants integrated with dense dislocations and (b) voids formed at GBs for TWIP steel deformed at 200 °C.

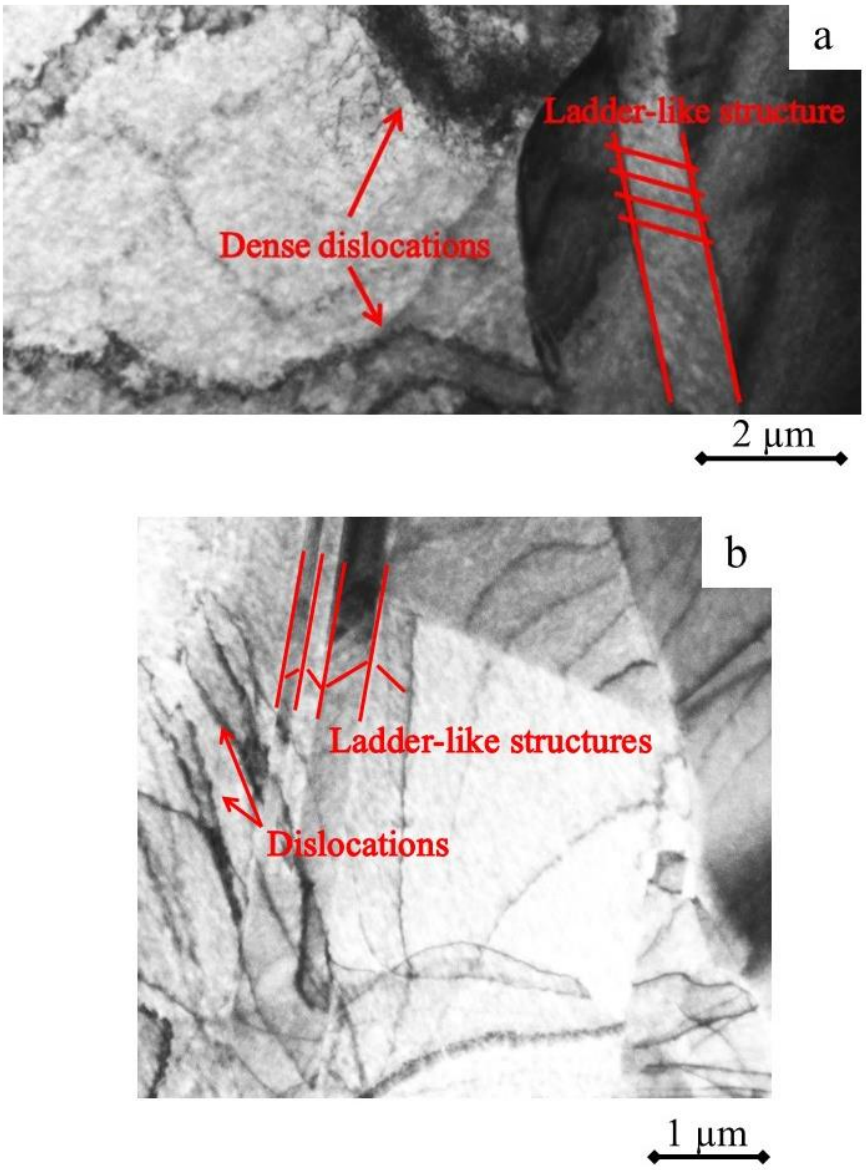

Figure 1.3.3 Microstructure of TWIP steel following deformation at (a) RT and (b) -170 °C: nano-twins inside primary twins forming ladder-like structures and dense dislocations are visible.

For the case of the XIP steel, of which the Mn content is higher, plastic deformation under impact loading was dictated mainly by dislocation glide at 200 °C as evidenced by vast amount of dislocations in Figure 1.3.4. This slip dominancy is caused by the increase in SFE as a result of the higher content of Mn. The increase in SFE increases the energy required for

abrupt change in the orientation due to twin nucleation. The higher SFE of XIP steel made twin formation possible only at low temperatures, i.e. RT (Figure 1.3.5) and -170 °C (Figure 1.3.6). Consequently, when temperature is lowered, slip activity was decreased and the plastic deformation was dominated by both twinning and slip. Along with the altered micro-mechanisms activated as temperature decreased, the twinning scheme also differed such that while two different twin variants were formed at RT (Figure 1.3.5(a)), nanoscale twins were formed inside preformed twins at -170 °C (Figure 1.3.6). The decrease in diffusion emerged by the decreased slip activity agrees well with a previous work where high-velocity, i.e. up to 20 m/s, tension tests were conducted [47]. The results revealed that the high speed of deformation inhibited dislocation activity and increased the twin density which improved the overall strength of the material [47]. Specifically, in the case of deformation at RT, two different twin variants were detected integrated with dislocations Figure 1.3.5(a). This deformation scenario consists of two twin variants together with slip lines was also forwarded in studies where room temperature uniaxial tension tests [17,48,77] and split-Hopkinson bar (SHB) tensile tests [65] were conducted on materials with close Mn content. However, the increased twin activity observed in the current work was the contrary to that of standard uniaxial tension tests [17,48,77] which was caused by increased speed of deformation due to impact loading. In addition to twinning response, the dislocation activity in the current study was similar to that of a previous work where high velocity SHB tension test was carried out [65] proving the decreased. Furthermore, the lowered slip activity related to decreased diffusion was also shown in a work where isothermal compressive tests were conducted on XIP steel [51]. The results indicated that the deformation was composed of two twin variants interacting with dislocation substructures [51]. This enhanced twinning observed in the current study due to a temperature decrease from RT to -170 °C was also in good agreement with a previous work where tension tests were carried out at the same temperatures and the

same increased twin activity was forwarded [44]. The lowered slip activity was related to the high speed of deformation in the current work due to limited movement of dislocations in the microstructure. On the other hand, along with the twin formation, voids were only observed at RT (Figure 1.3.5(b)). However, following more decrease in temperature down to -170 °C, nanoscale twins were formed within primary twins (Figure 1.3.6). This nanoscale twins were forwarded as well in a previous study [52]. Severe plastic deformation was applied via equal angular channel pressing at high temperatures [52]. The high temperature coming together with the severe loading improved dislocation activity [52], however, this temperature increase was not the case in the current study.

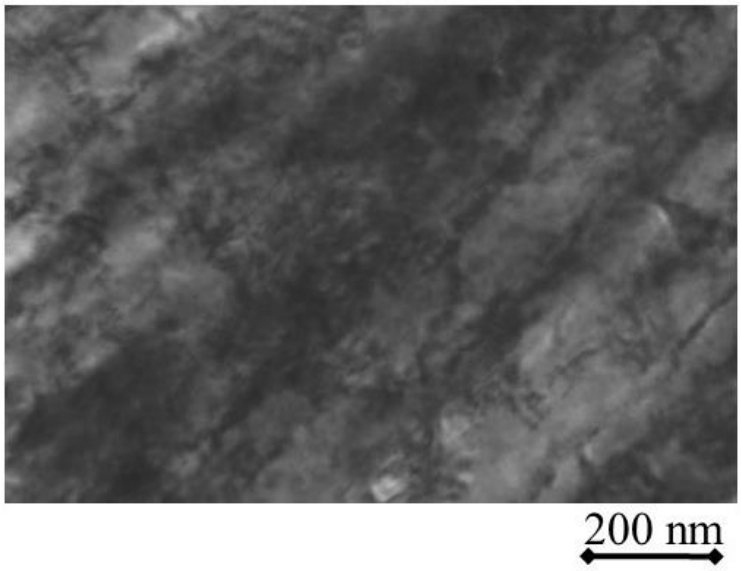

Figure 1.3.4 Microstructure of XIP steel deformed at 200 °C: dislocation slip dominates the microstructure.

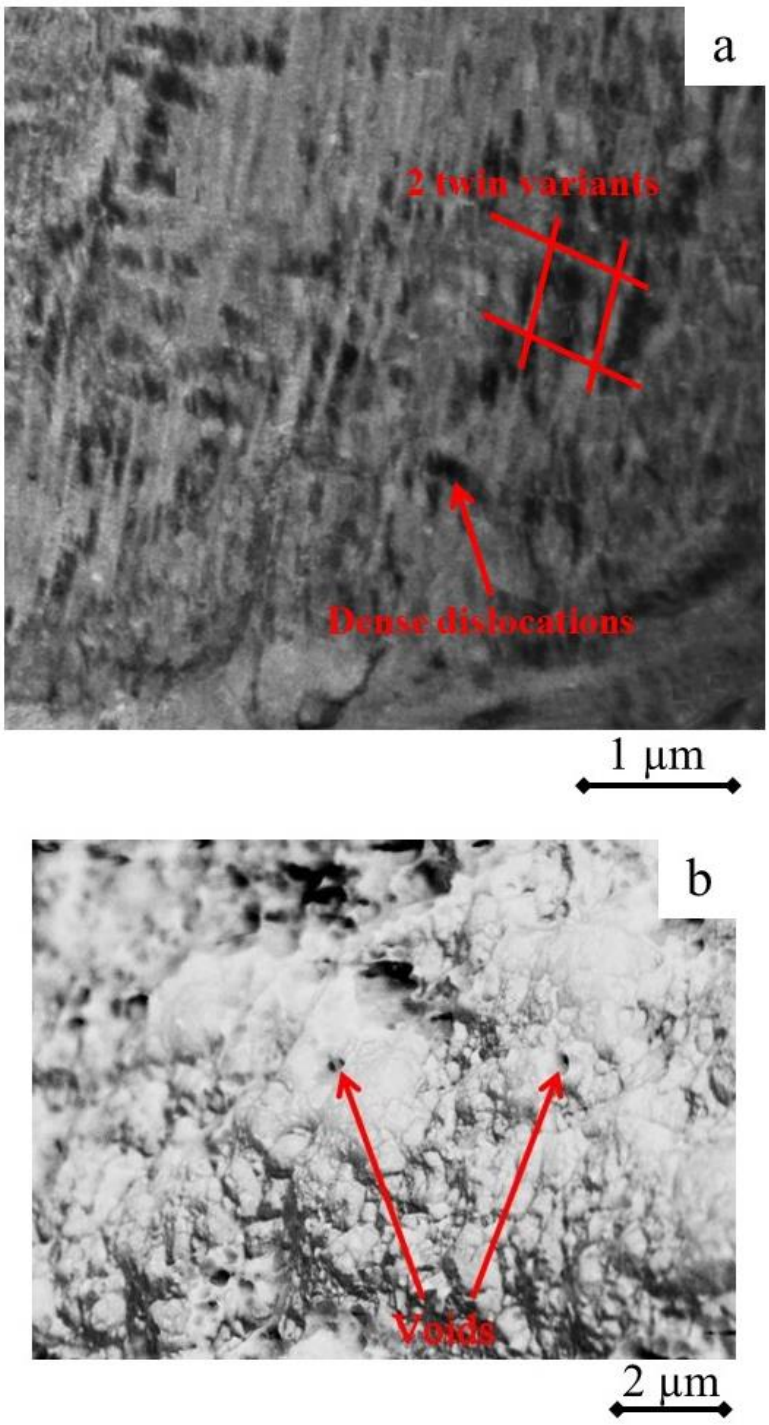

Figure 1.3.5 Microstructure of XIP steel deformed at RT: (a) Two different twin variants and dense dislocation structures within twins and (b) voids formed during deformation.

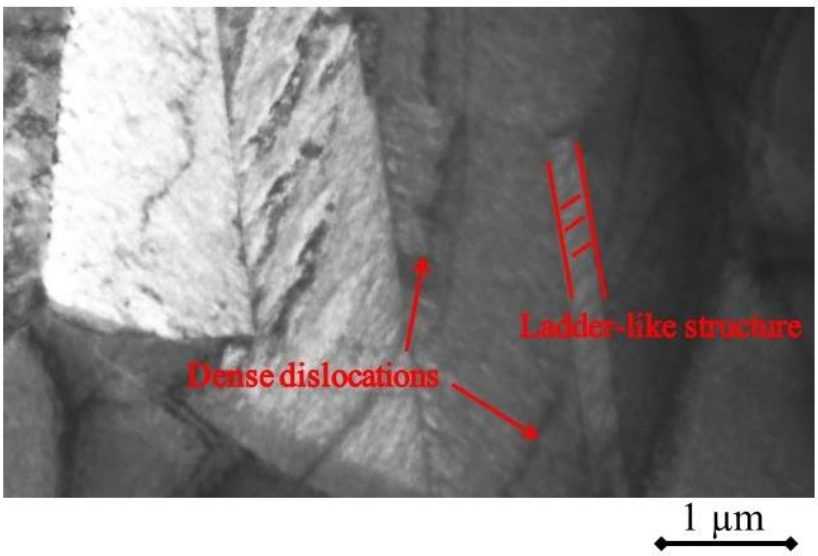

Figure 1.3.6 Dense dislocations and nano-twins that formed in XIP steel sample upon deformed at -170 °C.

1.2.2.2 Thermographical Analyses

In order to have a thermal perspective on the deformation behavior of both the TWIP and the XIP steels, experiments at 200 °C and RT were recorded by a thermal camera. The changes in the temperature of the samples during impact loading were analyzed at 200 °C and RT of which the results are plotted in Figures 1.3.7 and 1.3.8, respectively. The ductile and relatively more brittle fracture behaviors of XIP and TWIP steels were observed through the temperature distribution within the fracture zone, i.e. around the notch, during impact loading. For the case of 200 °C, the amount of increase in temperature of TWIP steel, i.e. 20 °C, is lower than that of XIP steel, i.e. about 60 °C. The reason why the increase in the temperature of XIP steel was higher is that there was only slip deformation while there were slip and twinning coexisting together for TWIP steel. The lack of micro deformation mechanisms activated at high temperatures in XIP steel made the given energy through impact loading not to be transferred into lattice distortion, instead it was transformed into heat resulting in more

increase in the temperature of the sample. However, for TWIP steel, there were twins and voids in addition to dislocation glide, hence the amount of energy dissipated through heating of the sample was lowered resulting in a smaller temperature increase of the sample. In contrast to the situation at 200 °C, at RT, both of the steels were deformed by twinning and slip, thus the increase in temperature of the sample during deformation was similar for both materials (about 80 °C).

In addition to these microstructural discussion on the changes in the temperatures of these materials, the differences in the increases in the temperature of the samples upon the hit of impact hammer could be tied up to the heat capacities of TWIP and XIP steels. Specifically, these two materials have different heat capacities than each other and these heat capacities are also a function of testing temperature. Hence, the thermal analyses may also be criticized from the heat capacity perspective. However, such a discussion including the heat capacities of these materials is beyond the scope of this study.

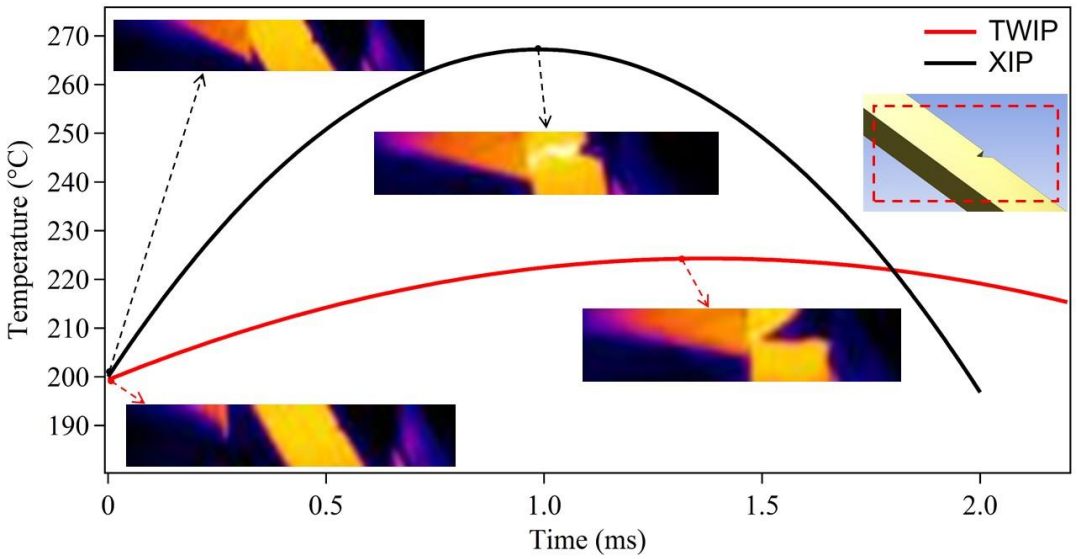

Figure 1.3.7 In-situ thermal analyses of impact deformation of TWIP and XIP steels at 200 °C. The inset indicates which location on the samples the thermographs correspond to.

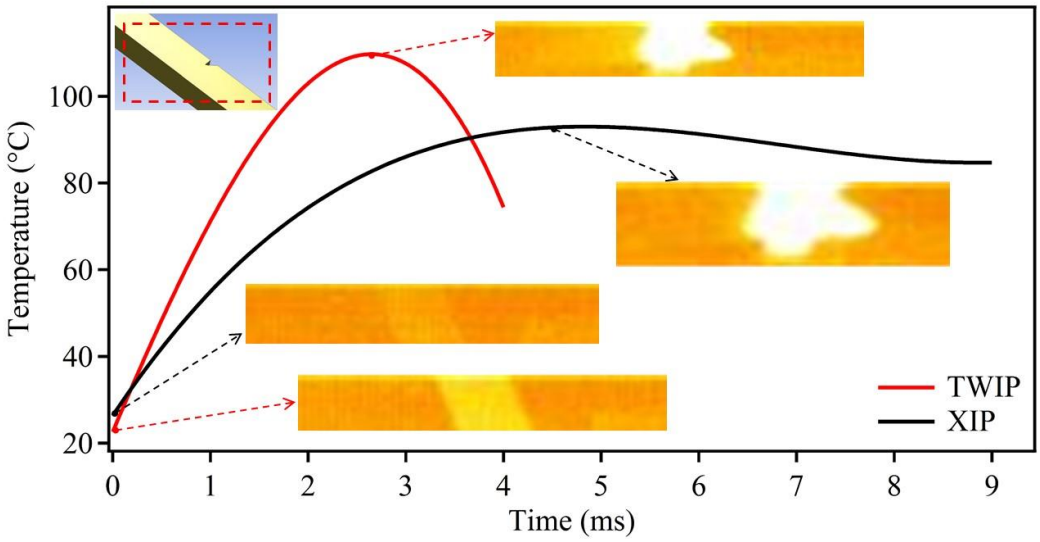

Figure 1.3.8 In-situ thermal analyses of impact deformation of TWIP and XIP steels at RT. The inset indicates which location on the samples the thermographs correspond to.

1.3.3 Summary

Overall, the results of the impact tests indicated the dependence of the mechanical response on the chemical composition since the active deformation mechanisms were observed to be different for two steels at the same test temperature. In addition to overall response, twinning scenario differed as well, such that with changing test temperature either different number of twin variants were activated or nano-scale twins were formed inside primary twins. On the other hand, as thermographical analyses revealed, the different deformation response of these two steels, i.e. different mechanisms activated upon loading, altered the increase in the temperature of the sample at the instant of impact until fracture. Specifically, more the micro-mechanisms involved in the plasticity of the material the less the increase in the temperature. However, all these results demonstrated the complicated deformation behavior of high-Mn steels. Therefore, the speed of deformation was increased via high-velocity compression tests as will be discussed in the following section.

1.4 INVESTIGATION OF TWINNING ACTIVITIES IN HIGH-Mn AUSTENITIC STEELS UNDER HIGH-VELOCITY COMPRESSIVE LOADING

1.4.1 Experimental Details

Since the impact tests has shown the requirement for more accelerated loading scenario to further simplify understanding the mechanical behavior of high-Mn steels, high-velocity compression tests with velocity range of 3-8 m/s were conducted on three different types of steels, namely, Hadfield, TWIP and XIP steels. The chemical compositions of these three steels are presented in Table 1.4.1. Surfaces of the samples were prepared by standard grinding and polishing metallographic equipment, and etched with a solution of 5% nitric acid in methanol for approximately 1 minute, and then cleaned with ethanol. Optical microscopy and stereographic microscopy were carried out to examine the surface microstructure prior to and following the experiments. SEM and TEM observations were performed in order to obtain detailed information about the TWIP effect and the states of micro-deformation mechanisms upon high-velocity compression experiments.

Table 1.4.1 Chemical compositions of studied materials (in wt.-%).

Steel	C	Si	Mn	Ni	Cr	V	Co	Ti	Fe
HS	1.090	0.432	12.340	0.148	0.297	0.035	0.044	0.007	Balance
TWIP	0.628	2.601	14.843	0.065	0.043	0.023	0.012	0.006	Balance
XIP	0.600	0.190	20.990	0.018	0.118	0.129	0.011	0.004	Balance

SEM investigations were carried out on a field emission scanning electron microscope while a TEM equipped with a 200 kV electron gun was utilized for the TEM analysis. For TEM work, thin foils were extracted from the samples in the form of flat disks with a

thickness of approximately 250 μm. These disks were then mechanically thinned down to 80 μm, and in order to obtain large electron-transparent areas, electropolished on both sides by conventional twin-jet electropolishing with an electrolyte consisting of 100 ml 40 % perchloric acid, 500 ml butoxyethanol and 400 ml 100 % acetic acid. The electropolishing was carried out at -20 °C under an acceleration voltage of 20.5 V.

For the high-velocity compression testing, 4 mm × 4 mm × 10 mm samples were extracted by electro-discharge machining. The compressive load was applied with a 3-kg hammer using a custom made experimental setup. The hammer was allowed to free fall from three different heights to achieve different deformation rates. The heights chosen for the experiments on Hadfield steel were 2, 2.75, and 3.5 meters, which correspond to velocities in the range of 6-8 m/s. On the other hand, the falling height for TWIP and XIP steels was chosen to be 0.5 meters, which is close to 3 m/s as deformation velocity. The velocity was kept at a smaller value for the TWIP and XIP steels due to the catastrophic damage on samples observed when the free fall was initiated at more than 3 m.

In order to detect temperature effects, experiments were conducted at three different temperatures: -170 ºC, RT, and 200 ºC. The sample surfaces were subjected to metallographic preparation prior to experiments to be able to take confocal microscopy images after the tests. During the experiments, temperature of the samples was recorded by a thermographical camera, which helps tracking the temperature increase during abrupt loading.

1.4.2 Results and Discussion

1.4.2.1 Microstructural Analyses

The mechanical behavior of all three materials is summarized in Table 1.4.2 based on the active mechanisms observed at each temperature. The investigations on the lowest Mn-containing sample, i.e. Hadfield steel, revealed that slip, twinning, twinning inside primary

twins, slip bands inside twins, and voids were prevalent at all temperatures, as illustrated in Figure 1.4.1. The observed twinning scenario, where two different twin variants were activated during plastic deformation, was also reported previously, where Hadfield single crystals were deformed under uniaxial tensile [8] and compressive [7] loading, such that two dominant twin systems and dislocation glide were simultaneously active. In addition to these examples where the deformation was imposed at relatively moderate strain rates, the deformations applied at high strain rates, such as high-pressure torsion experiments [29], were also dictated by two active twin systems.

Table 1.4.2 Active deformation mechanisms in the current materials at different temperatures.

	200 °C	**RT**	**-170 °C**
HS	S, ST ,T , V, TT	S, ST ,T , V, TT	S, ST ,T , V, TT
TWIP	2 T, S	TT, S	TT, S
XIP	S	3 T, TT, S	2 T, S

S: slip ***T: twin*** ***TT: twin-inside-twin*** ***ST: slip-inside-twin*** ***V: void***

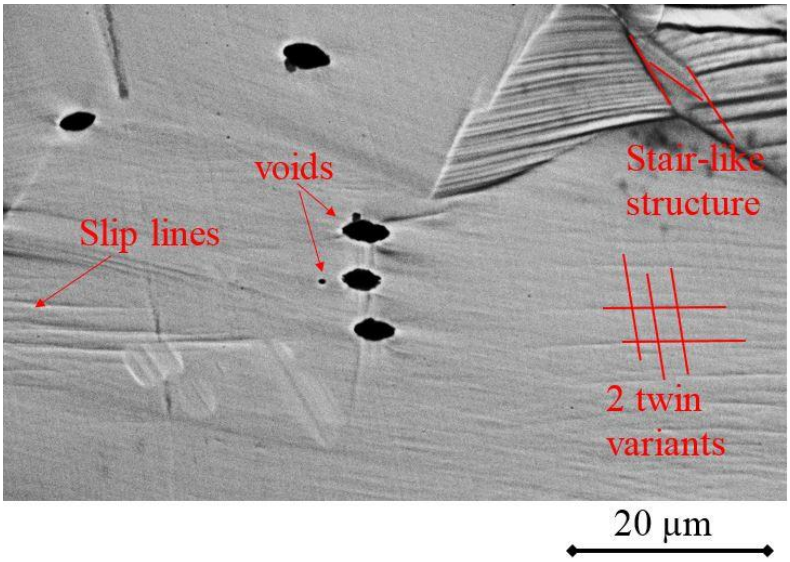

Figure 1.4.1 SEM image of Hadfield steel deformed at RT: slip lines, voids, stair-like twinning and two different twin variants are visible.

Another notable finding about Hadfield steel was the change in slip line width, in other words the mean distance between dislocations gliding on parallel systems, where slip dislocations crossed the twin boundaries, as shown in Figure 1.4.2: the distance between subsequent slip lines differed when the glide dislocations interacted with the boundaries of deformation twins. This phenomenon stands in good agreement with the results previously forwarded by Shen et al., where the twin width changed after cutting through another twin boundary on a different system [16]. Similarly, the change in slip line width in the current study can be attributed to the dissociation of glide dislocations into partials when crossing a twin boundary [16]. Specifically, the formation of secondary micro-twins not only decreases the mean-free path of dislocations but also increases the energy barrier to be exceeded by dislocations to cut through a twin boundary, which is hard to achieve in a coarse-grained materials. However, the presence of multiple twins and micro-twins forming in between twins act in such a way that each grain indeed consists of many sub-grains, enabling the dislocations to attain much higher energy levels that are large enough to promote their dissociation into Shockley partials as they cut through twin boundaries [16].

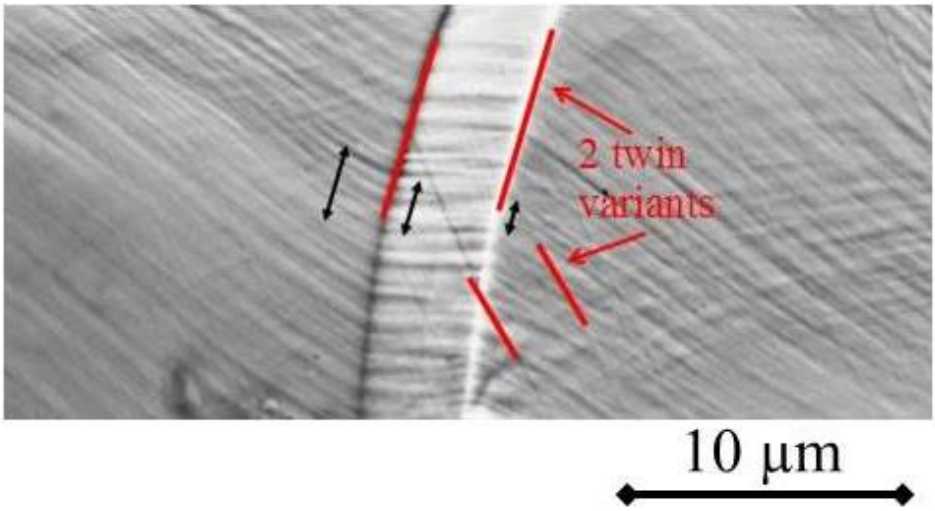

Figure 1.4.2 The change in slip line width crossing a twin boundary.

A comparison of results on the deformation responses of Hadfield steel at 200 °C and -170 °C revealed that increased twinning activity was prevalent at -170 °C, which indeed resulted in a more brittle fracture as evident from the stereographic micrographs (Figure 1.4.3). This brittle behavior stemming from enhanced twinning agrees well with previous results obtained from impact experiments carried out on Hadfield steel at temperatures below 0 °C and deformation velocities similar to those employed in the present study [36]. The ductile to brittle transition was shown to take place between -100 and 50 °C [36], indicating that the observed brittle behavior is brought about by increased twinning activity, resulting in enhanced slip-twin interactions during plastic deformation. The surface relief of the fracture surface of Hadfield steel deformed at -170 °C can be seen in Figure 1.4.4, which illustrates the more brittle deformation behavior due to enhanced twinning activity and slip-twin interactions.

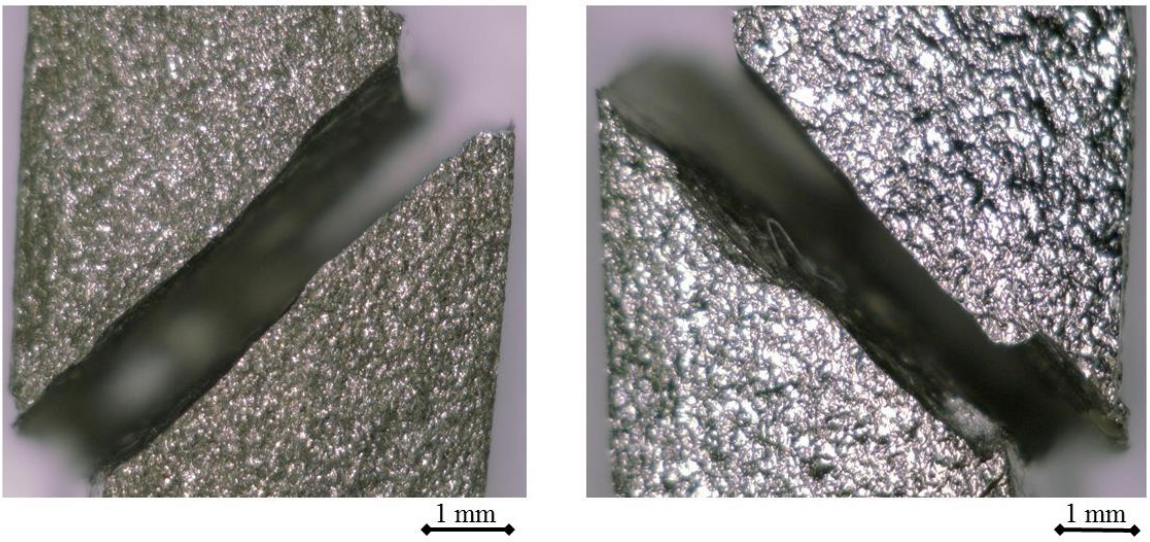

Figure 1.4.3 Optical micrographs of brittle fracture of Hadfield steel, where the hammer fell from 2.75 m and the temperature was -170 °C.

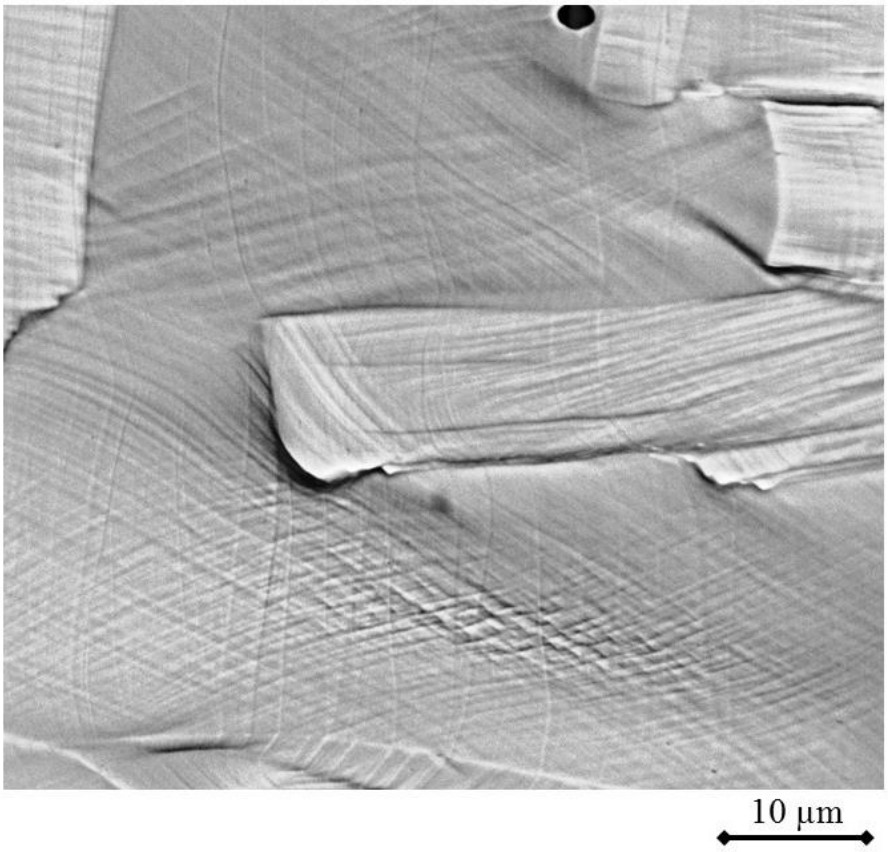

Figure 1.4.4 Interacting twin-slip structures of Hadfield steel when deformed at -170 °C resulting in enhanced surface relief.

The Si-containing samples, i.e. the TWIP steel samples, exhibited different types of twinning activity depending on the test temperature: at 200 °C, two different twin variants were activated (Figure 1.4.5), while nano-twin formation inside previously formed twins was observed by a decrease in temperature down to RT (Figure 1.4.6(a)). This nano-twin formation inside thick primary twins was previously reported, where severe plastic deformation was imposed upon samples at elevated temperatures [52]. Although the higher temperatures promote diffusion, which may result in decreased twinning activity over dislocation glide, the nano-twin formation was still prevalent, which was attributed to the low SFE of TWIP steel, which makes the abrupt orientation change due to twin formation easier. Further decrease in temperature down to -170 °C made the dislocation activity less

pronounced due to decreased atomic diffusion rate at low temperatures (Figure 1.4.6(b)) [36]. The difference in Mn content of TWIP steel (≈15% Mn) as compared to that of Hadfield steel (≈12% Mn) is responsible for the decrease in SFE, which results in more enhanced twinning activity as it was the case in this study (≈15% Mn) and in an earlier work (≈18% Mn) [33], where the number of active twin systems increased concomitant with strain.

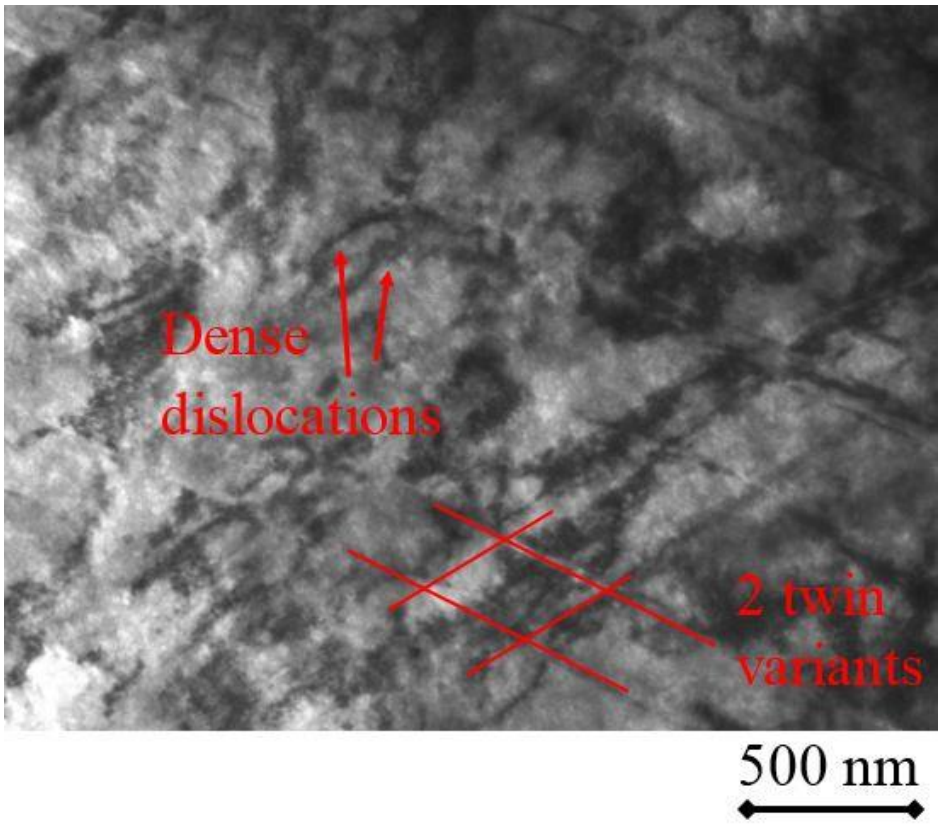

Figure 1.4.5 TEM image of TWIP steel deformed at 200 °C: two different twin variants and dense dislocation structures are visible.

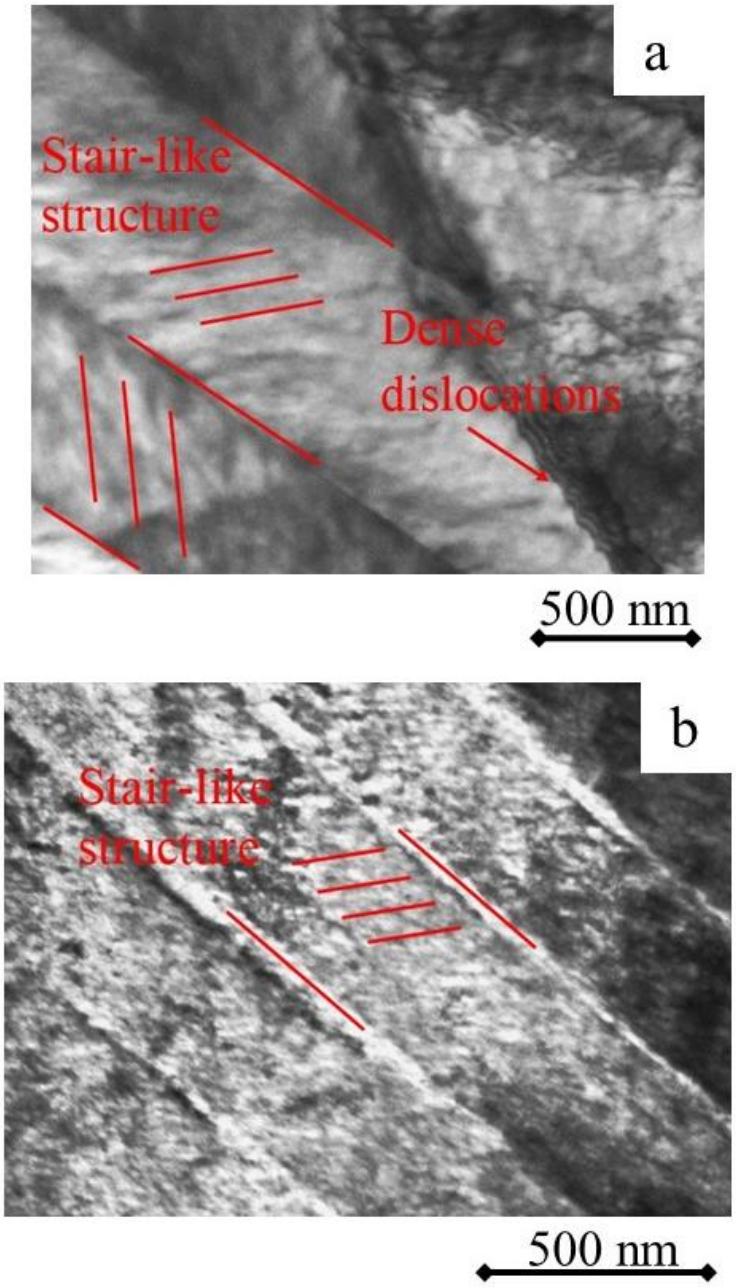

Figure 1.4.6 TEM images of TWIP steel deformed at (a) RT and (b) -170 °C.

The highest Mn-containing material, i.e. the XIP steel, on the other hand, deformed mainly by slip at 200 °C as shown in Figure 1.4.7. At lower temperatures, different twin variants were active in this material in addition to dislocation slip, which was observed as integrated twin networks within the microstructure (Figure 1.4.8). The variety of active microdeformation mechanisms was well verified in literature on samples with closer Mn

contents to that of XIP steel [17,48,51]. There are two twin variants and dense dislocation activities observed in the microstructure of the sample where low strain rate tensile deformation was carried out at room temperature [17,48]. However, the third twin variant and dislocation-twin interaction was not reported due to low velocity of tensile deformation as opposed to the faster deformation in the current study, which triggers these additional mechanisms and interactions. Despite the fact that a higher strain rate was applied in compression tests in the work of Steinmetz et al. [51], the reported mechanisms were again limited to two different twin variants and dislocation cells, as revealed by the observations made following the experiments conducted at temperatures ranging from RT to 600 °C. This implies that the third twin variant observed in the current study was a result of higher deformation velocity applied. Specifically, as the strain rate increased, the contribution of the atomic diffusion further diminished, promoting the activation of the third twin variant.

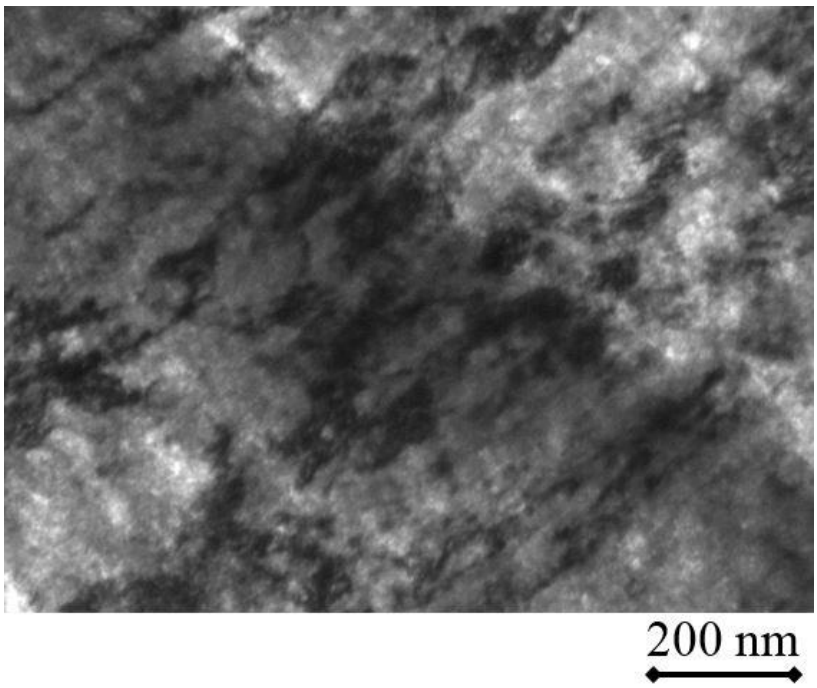

Figure 1.4.7 TEM image of XIP sample deformed at 200 °C,where only dislocation activity was observed.

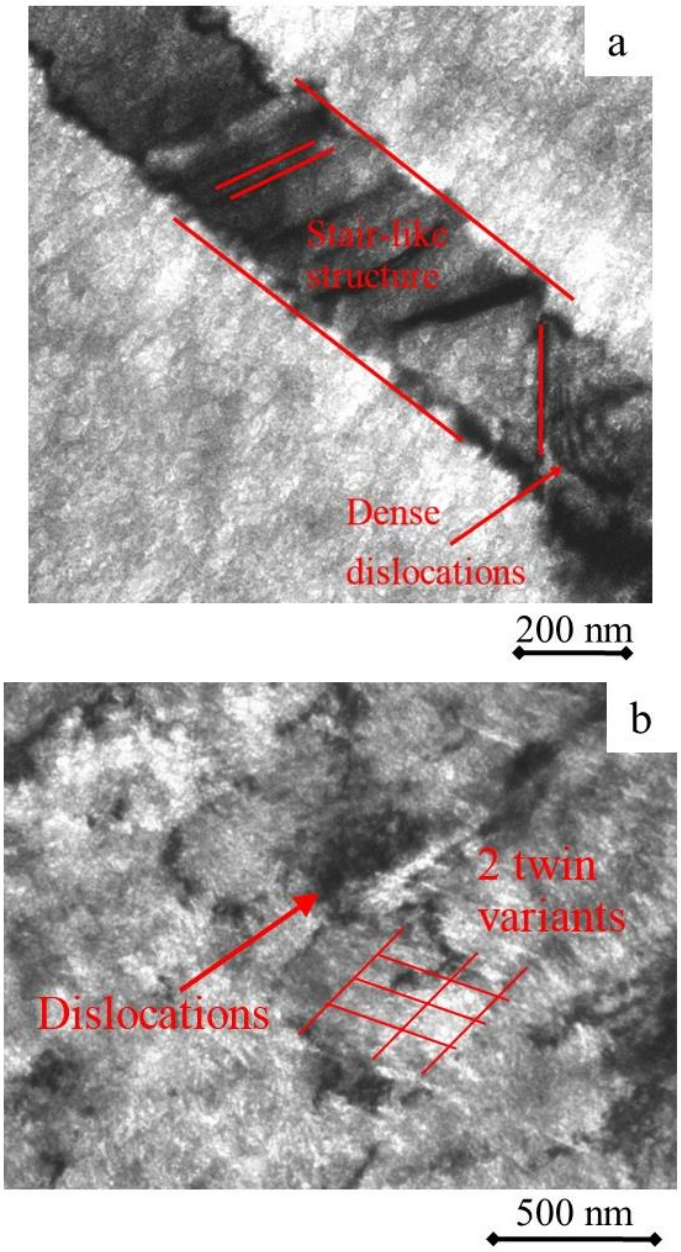

Figure 1.4.8 TEM images of XIP sample deformed at (a) RT and (b) -170 °C: different twin variants and high dislocation density are evident.

A comparison of the microstructures of deformed Hadfield and TWIP steels reveals that a variety of micro-deformation mechanisms dictate the plasticity of Hadfield steel as evidenced by the enhanced surface relief resulting from slip-twin interactions and voids (Figures 1.4.1 and 1.4.4). However, even though the Mn content in TWIP steel is very close to that of Hadfield steel, voids and interacting slip dislocations and twin boundaries were not

observed. This is attributed to the additional Si, which further decreases the SFE of TWIP steel, and thereby makes twinning more dominant, suppressing slip deformation. Moreover, the complexity of twin structures increased as deformation temperature decreased in TWIP steel, since slip deformation was eliminated owing to lowered diffusion rate (Figure 1.4.6(a)). Finally, when temperature decreased down to -170 °C, the slip capacity became so low that dense dislocation activity was not prevalent (Figure 1.4.6(b)).

The Mn content of XIP steel (about 21%) is significantly higher than those of TWIP and Hadfield steels (about 15% and 12%, respectively), and this increase in Mn content causes the SFE to increase. This phenomenon was also observed in a previous study [11], where SFE decreased and then increased when the Mn content changed from 25% to 27%, and then to 28%. Even though the Mn contents of the current materials are different, the same Mn-content-dependent SFE trend was seen. Specifically, the increase in SFE resulted in enhanced slip activity during plastic deformation (Figure 1.4.7). However, as temperature decreased to RT, twins and slip-twin interactions were prevalent (Figure 1.4.8(a)). Further decrease to -170 °C almost completely suppressed dislocation motion and two different twin variants dictated plastic deformation (Figure 1.4.8(b)). This unusual twinning activity with higher Mn content can be linked to the extremely low rate of diffusion at low temperatures and very high deformation velocity, such that the decreased atomic diffusion rate inhibits dislocation glide, favoring plastic deformation by twinning over slip.

Overall, the current results demonstrate the significant dependence of twinning activity on loading velocity and chemical composition for three different high-Mn austenitic steels. The important finding is that high velocity of deformation at low temperatures promotes nano-twin formation in high-Mn austenitic steels, which significantly contributes to the exceptional work hardening capacity of this class of steels. Formation of nano-twins also exhibits dependence on the alloy content, such that nano-twins formed in Hadfield steel at all

temperatures, while they were prevalent only at low and intermediate temperatures in TWIP and XIP steels, respectively. Specifically, the nano-twins forming within previously formed twins create stair-like structures, which contribute to the overall work hardening of high-Mn steels by providing additional barriers against dislocation glide. Henceforth, the current set of experimental results provide important clues to the enhancing of work hardening capacity of high-Mn steels by controlling the alloy composition for a given service temperature.

1.4.2.2 Confocal Microscopy Analyses

The experiments were conducted at three different temperature - deformation energy combinations, where the energy of deformation was dictated by the falling height of the hammer, in order to promote significantly different twinning activities: -170 °C and 3.5 m (Case-1), room temperature (RT) and 2.75 m (Case-2), and 200 °C and 2 m (Case-3), such that deformation velocities within the range of 6-8 m/s were attained. The microstructures of deformed samples were examined by post-deformation CLSM. The experimental results for selected cases that emphasize the roles of increasing deformation velocity and decreasing temperature are presented. Accordingly, plastic deformation in Case-1 is facilitated by two different twin systems that interact with glide dislocations on active slip systems, which coexisted with concentrated slip lines around voids in the microstructure (Figure 1.4.9). These initial results agree well with the previously forwarded findings on Hadfield steel samples subjected to high-strain rate Charpy impact tests, where the interaction of slip and twinning in the presence of slip lines piling up around voids due to increased twin activity was prevalent at subzero temperatures [36]. Similar observations were also reported upon ultra-high velocity deformations of Hadfield steel utilizing split-Hopkinson bar experiments, such that both twinning activity and work hardening capacity of Hadfield steel increased concomitant with strain rate [78].

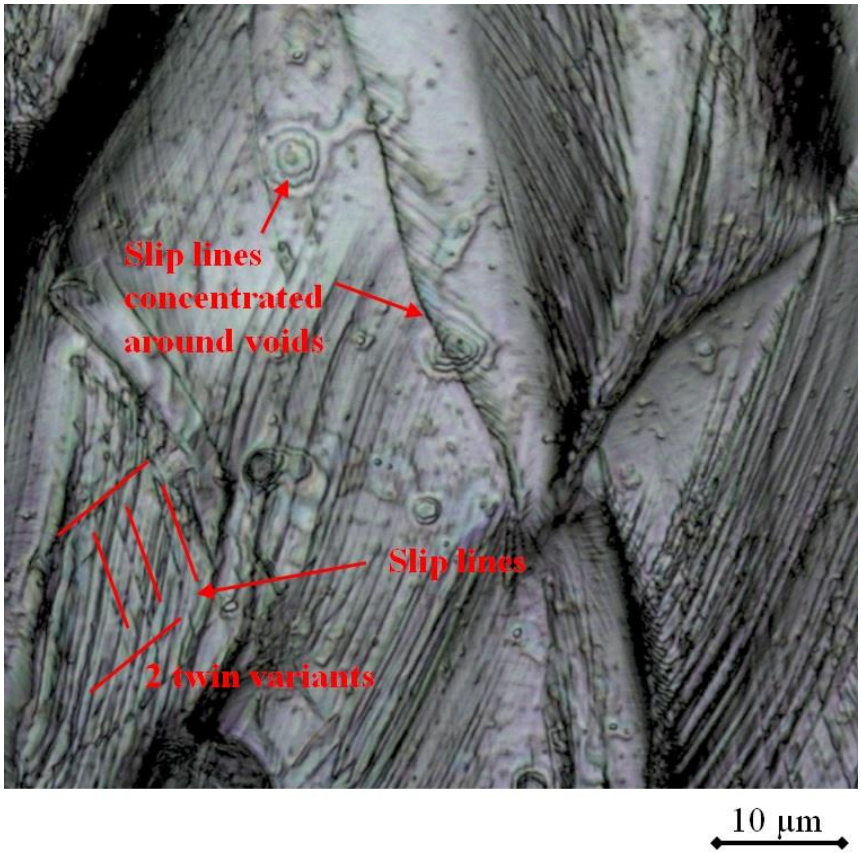

Figure 1.4.9 CLSM-image of the of the post-deformation surface appearance of the Case-1 sample revealing the presence of coexisting twins, slip lines and voids.

In addition to the aforementioned observations that agree well with the literature, an additional mechanism was also prevalent in the microstructure of the Case-1 samples: nano-twin formation within micro-scale primary twins was evident throughout the microstructure, as also supported by the CLSM profile analysis (Figures 1.4.10 and 1.4.11). For instance, the surface profile presented in Figure 1.4.11 shows a number of steps within the micro-scale primary twins shown in Figure 1.4.10, and three of these segments are indicated with lines of different colors, which correspond to nano-scale twins with a thickness of about 4 nm. These nano-scale twins can be compared to second order micro-scale twins observed that form within secondary twins in Hadfield steel (with a very similar chemical composition to the

current material) monotonically deformed at RT and relatively slower strain rates [57], such that both mechanisms increase the work hardening capacity of the material. However, the size of the second-order twins decreased down to 4 nm in the current work, indicating the significant effects of simultaneously increased strain rate and decreased deformation temperature. In particular, these extreme boundary conditions restrict the dislocation glide, and the material deforms plastically mainly on primary twins and the nano-scale twins that form within.

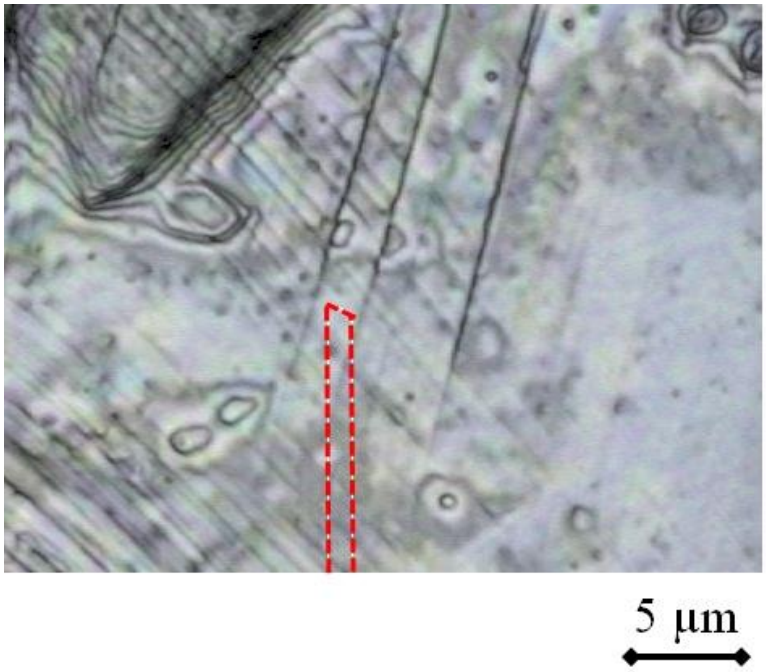

Figure 1.4.10 The post-deformation topography of the Case-1 sample. The section indicated by dashed red lines was subjected to surface profiling by CLSM (Figure 1.4.11).

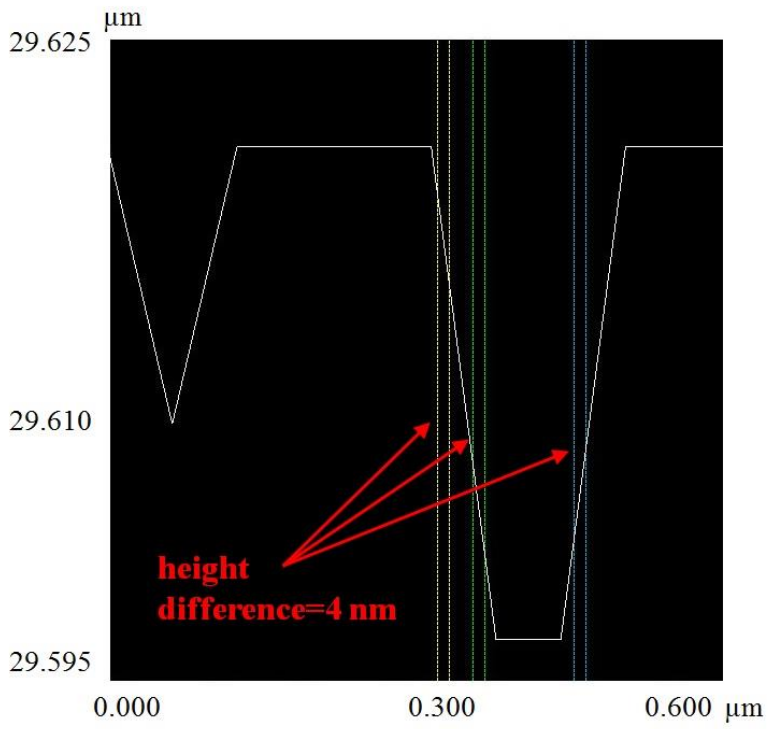

Figure 1.4.11 The CLSM surface profile of the marked section in Figure 1.4.10, showing nanotwins featuring a height difference of 4 nm within a primary twin.

When the deformation of Case-1 samples (Figure 1.4.12(a)) is compared to those of Case-2 (Figure 1.4.12(b)) and Case-3 (Figure 1.4.12(c)), all twinning, slip and void formation are present in the microstructures, yet with different relative fractions (Figure 1.4.12). Specifically, increasing deformation temperature and decreasing deformation velocity promote atomic movements over lattice reorientation, which means that dislocation glide is preferred over twinning. In Case-1 (Figure 1.4.12(a)), where the twin density is the highest, the twin boundaries act as effective barriers against dislocation motion during plastic deformation [36], and the glide dislocations pile up around voids in the microstructure (Figure 1.3.9). When the twin activity is less, such as in Case-2 and Case-3 samples, the slip lines are spread all over the microstructure (Figures 1.3.12(b) and (c)) instead of localizing around voids as the dislocations encounter less twin boundaries hindering their motion.

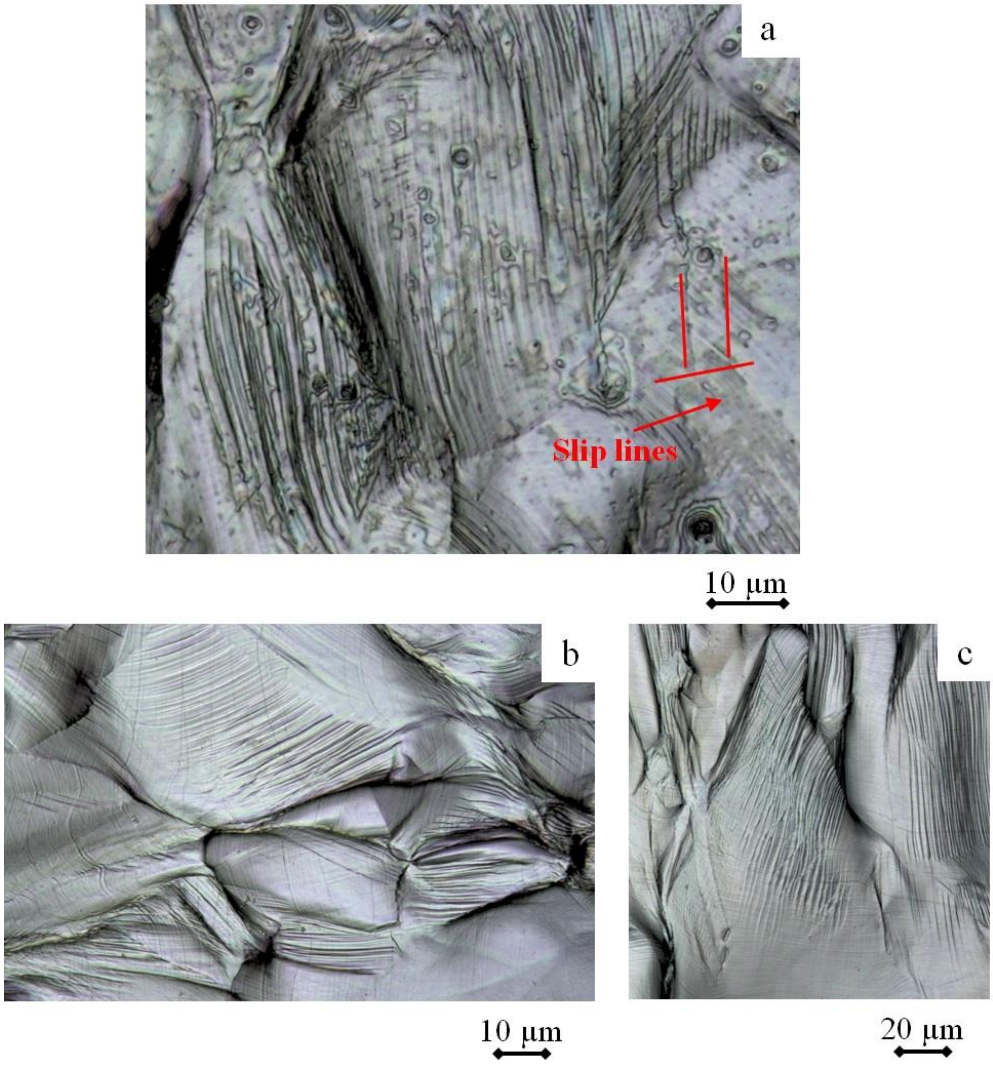

Figure 1.4.12 A comparison of relative twin activity evident in (a) Case-1, (b) Case-2, and (c) Case-3.

1.4.3 Summary

Overall, the current set of results evidence that it is possible to further improve the work hardening capacity of high-Mn austenitic steels by tailoring the parameters, such as temperature, deformation velocity and alloy content, all of which dictate the twinning activity in this class of materials. However, it was still not possible to comprehend the complex mechanical response of high-Mn steels. Thus, a further accelerated split-Hopkinson bar (SHB) tensile tests were conducted which will be demonstrated in the following section.

1.5 TWINNING ACTIVITY IN HIGH-MANGANESE AUSTENITIC STEELS UNDER HIGH -VELOCITY LOADING

1.5.1 Experimental Details

Following the high-velocity compression tests, a more accelerated loading scheme, i.e. split-Hopkinson bar (SHB) tension, was applied on the TWIP (15 wt. % Mn, 0.6 wt. % C, and 2.6 wt. % Si) and the XIP (21 wt. % Mn and 0.6 wt. % C) steels at three temperatures, -170 °C, RT, and 200 °C. The test setup and the geometry of the samples tested is given in Figure 1.5.1 of which the thickness is 1.6 mm. Post deformation transmission electron microscopy (TEM) analyses were carried out.

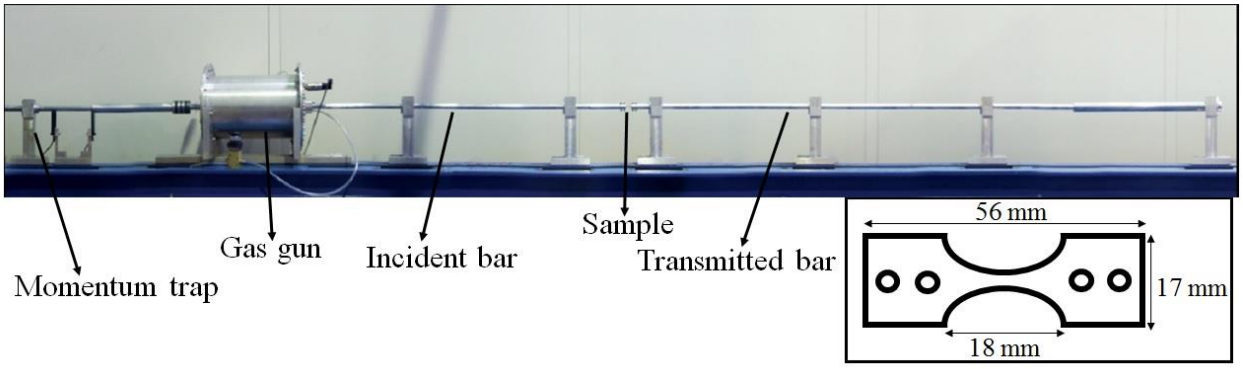

Figure 1.5.1 The SHB setup utilized in the current work. The inset shows the sample dimensions.

1.5.2 Results and Discussion

The active deformation mechanisms were tabulated at all three temperatures for both steels in Table 1.5.1 at each temperature. The deformation of TWIP steel consisted twins at all the three temperatures; however, the scenario at each one was considerably different.

Table 1.5.1 Dominating deformation mechanisms observed at all temperatures for both steels.

	200 °C	**RT**	**-170 °C**
TWIP	2 T, S	TT, S	TT, S
XIP	S	T, S	TT, S
S: slip	***T: twin***	***TT: twin-inside-twin***	

Specifically, while two twin variants were observed at 200 °C (Figure 1.5.2), nanoscale twins were formed within previously formed twins at RT (Figure 1.5.3(a)) and at -170 °C (Figure 1.5.4). The RT case worth especially investigating thoroughly since the formation of nano-twins resulting in the ladder-like structure is also visible at the macro-scale fracture surface (Figure 1.5.3(b)). This is attributed to the extensive formation of ladder-like structures on parallel planes at the micro-scale, which emerges at the fracture surface at the macro-scale due to stress relief. Additionally, notable slip activity was also detected at RT, in spite of the low SFE at low temperatures and high speed deformation realized by the SHB. This surprising slip activity is associated with the increased thermal energy due to rapid lattice reorientation. Although this notable slip activity was still evident, it was relatively decreased when the temperature was lowered from RT to -170 °C (Figure 1.5.2-1.5.4).

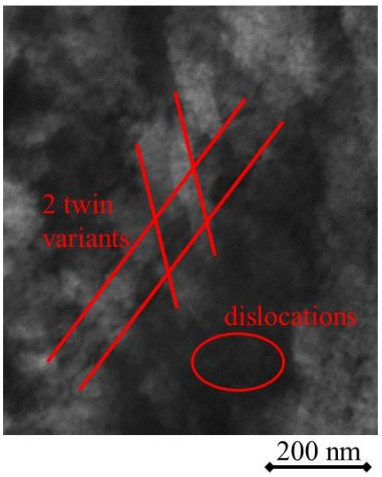

Figure 1.5.2 TEM bright-field image of TWIP steel deformed at 200 °C: two different twin variants and dense dislocation activity are prevalent.

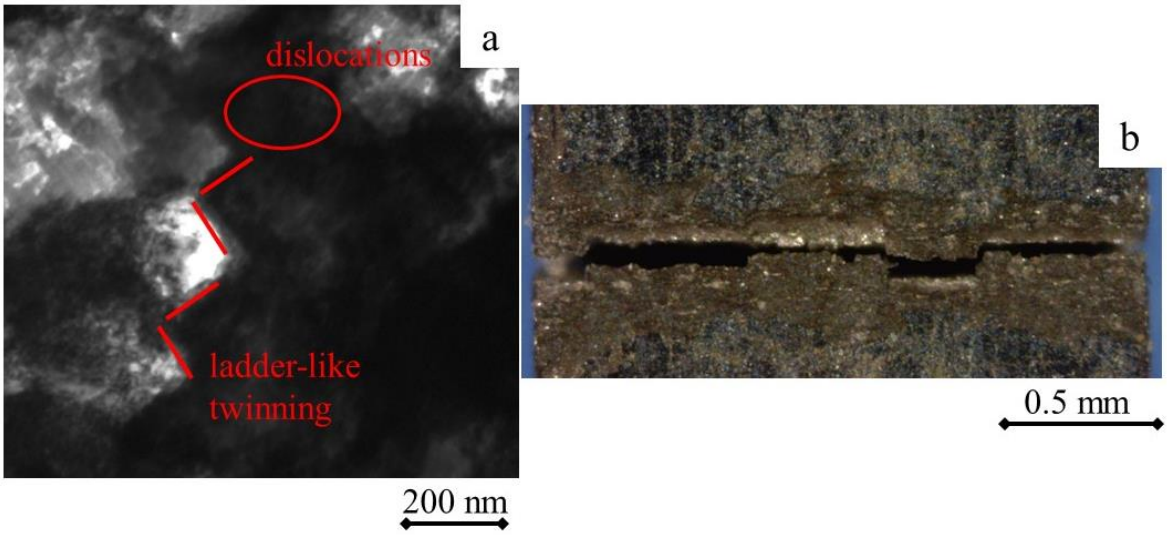

Figure 1.5.3 (a) TEM micrograph of TWIP steel deformed at RT showing ladder-like twin structures and dislocation clouds, (b) macro-scale fractograph of TWIP steel.

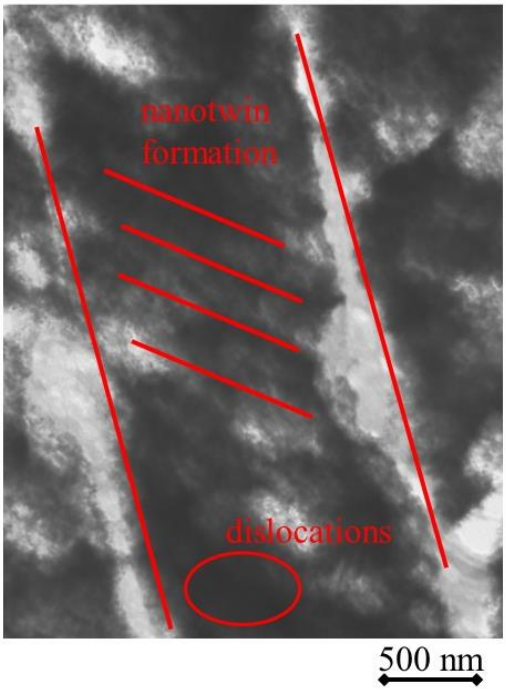

Figure 1.5.4 TEM image showing nano-twin formation within primary twins in TWIP steel deformed at -170 °C.

For the XIP steel of which the Mn content is higher, on the other hand, the elevated temperature plastic deformation was mainly dictated by dislocation glide as a result of higher SFE [11]. However, when temperature was lowered down to RT, one twin variant was

activated along with the dense dislocation activity (Figure 1.5.5), which disagree with a previous study where two active twin variants interacting with dislocations were forwarded for a steel with close Mn content to the XIP [79]. Particularly, the additional Al content of the steel utilized compared to XIP was further decreased the SFE of the material which resulted in a more pronounced twinning activity upon applied compressive load via SHB [79]. The deformation response of XIP steel revealed lower twinning activity by increased SFE due to higher Mn content of XIP steel than in TWIP steel, which stands in good agreement with the previously reported unusual Mn-content dependence of SFE in high-Mn austenitic steels [11]. When the temperature was lowered even down to -170 °C, nanoscale twins were observed to be formed inside primarily formed twins (Figure 1.5.6). This unusual twinning scenario interacting with dislocations was the result of sustained atomic displacements in the lattice due to increased thermal energy upon high speed loading (Figure 1.5.6). Since the SFE of XIP steel is higher than that of TWIP steel, slip activity was not affected significantly by the temperature change as higher SFE of the material makes abrupt lattice movements associated with twin formation difficult.

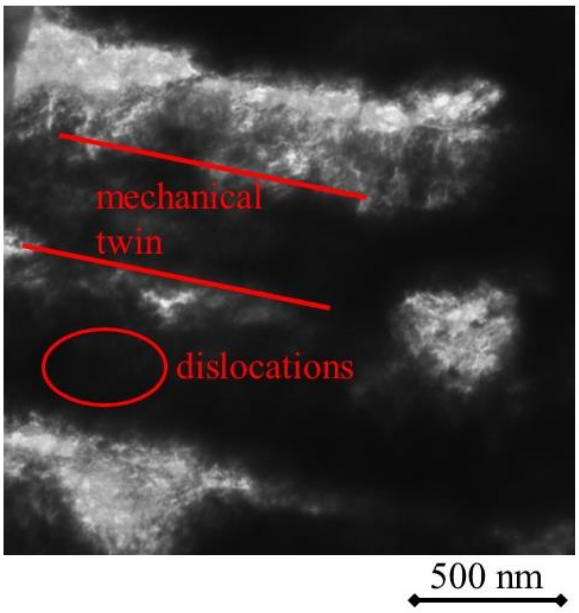

Figure 1.5.5 Twins and dislocations coexist in XIP steel deformed at RT.

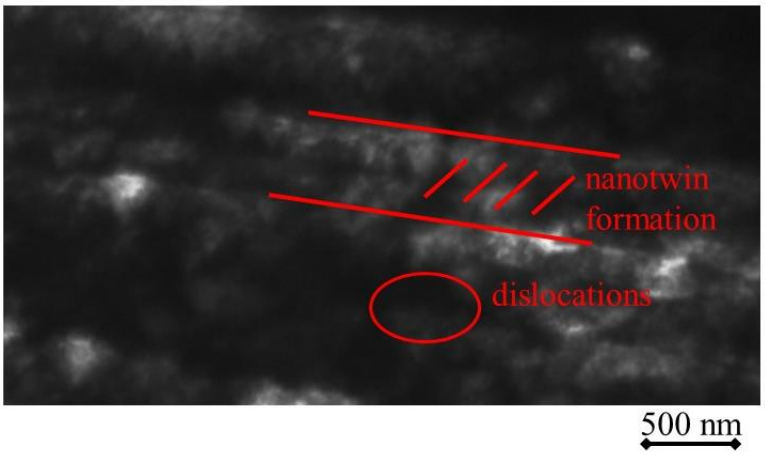

Figure 1.5.6 The nano-twin formation inside primary twins and dislocation substructures in XIP steel deformed at -170 °C.

1.5.3 Summary

Overall, including the SHB tests, the whole experimental effort clearly demonstrated the complicated deformation response of high-Mn austenitic steels where twinning plays a critical role together with other competing micromechanisms, such as grain boundaries.

1.6 CONCLUSION AND FUTURE WORK

The effect of GBMA on the mechanical response of high-Mn austenitic steels was investigated with the aid of MD simulations utilizing the LAMMPS algorithm. For this purpose, tensile deformation was simulated initially on copper and iron samples in order to simplify the simulations which have the length of 50 nm. First, two grains with misorientation angles of 2.5 to 67.5 degrees in between them were simulated. After the preliminary examination of two-grained samples, analyses were extended to a larger structure with seven grains. The misorientation angles in this case were implemented via rotation of the six grains surrounding the middle one. The results demonstrated the contradicting response of these two materials in terms of the effect of increasing GBMA when compared to experimental findings and numerical results at macroscale. Specifically, the tensile strength of both copper and iron decreased with increasing GBMA. On the other hand, the experimental results together with numerical analyses at macroscale have shown the increase in the material's strength with increasing GBMA. Therefore, the current study was broadened with experimental effort to clarify the response at micro-scale and observe all the mechanisms affecting the mechanical behavior of high-Mn austenitic steels.

The microstructure of high-Mn austenitic steels was examined comprehensively in terms of the effects of chemical composition and deformation temperature on micro-scale deformation response of these materials. In terms of chemical composition, three types of steels were tested with different alloy content, while the experiments were conducted at three different temperatures. High-velocity loading schemes were considered, namely impact, high-velocity compression and ultra-high-velocity tension. The motivation behind these high deformation velocities was to promote twinning over other mechanisms such as dislocation glide and slip-twin interactions. In order to investigate the micro-mechanisms activated during deformation, scanning electron microscopy and transmission electron microscopy were

utilized on both as-is and deformed samples. In addition, confocal laser scanning microscopy and thermographical analyses were carried out for compressive deformation of Hadfield steel and impact deformation of TWIP and XIP steels, respectively. The results have shown that high deformation velocity and low temperatures favor nano-twin formation in high-Mn austenitic steels, which significantly contributes to strain hardening. Formation of nano-twins also depends on the alloy content, such that nano-twins formed in Hadfield steel at all temperatures, while they were prevalent only at low and intermediate temperatures in XIP and TWIP steels, respectively. Overall, the current set of results evidence that it is possible to further improve the work hardening capacity of high-Mn austenitic steels by tailoring the parameters, such as temperature, deformation velocity and alloy content, all of which dictate the twinning activity in this class of materials. Moreover, from a thermal perspective, as analyses on impact response have revealed, when both twinning and dislocation glide take place the increase in the temperature of the sample due to impact deformation was lower than that in the case where only slip was active. This was attributed to the larger amount of energy transformed into lattice movements instead of the heating of the sample.

Overall, the first part of this thesis lays out the significance of each micro-mechanism activated during plastic deformation on the work hardening of high-Mn steels experimentally. However, the computational examination of the effect of GBMA on the work hardening of metals was left for future work. The examination will include the incorporation of all the micro-deformation mechanisms in simple structures, i.e. copper and iron, than the implementation of the same computational approach to high-Mn austenitic steels. For this implementation procedure, first fcc-iron may be chosen as the matrix material in order to simplify the simulations. In the future, other alloying elements present in the specific type of high-Mn steel can be incorporated into the lattice.

PART 2: THE ROLE OF TWINNING ACTIVITIES IN THE PSEUDOELASTICITY OF NiTi ALLOYS AND THEIR APPLICATIONS IN DENTISTRY

2.1 INTRODUCTION

2.1.1 Motivation and Background

In the previous part of this thesis, the importance of twinning in the deformation response of high-Mn steels was well demonstrated. Another phenomenon where twins play an active role in is the solid-to-solid phase transformation in metallic materials where twinning induced by straining results in a phase change within the microstructure. The common example of this solid state phase transformation is in shape memory alloys (SMAs) [80–82], while rare examples were also forwarded in some other alloys [83].

The SMAs exhibit three distinct types of behaviors that take place by diffusionless martensitic solid-to-solid phase transformation: one-way shape memory effect, two-way shape memory effect, and pseudoelasticity (Figure 2.1.1). In one way shape memory effect, the material has a certain crystal structure at micro-scale, i.e. a certain shape at the macro-scale, at its austenitic state to which it returns upon heating after applied plastic deformation resulting in a shape change (Figure 2.1.1(a)). On the other hand, in two-way shape memory effect, material has two corresponding crystal structures at both austenitic and martensitic states. Therefore, it is possible to interchange between two different macroscopic shapes upon heating and cooling of the sample (Figure 2.1.1(a)). The pseudoelasticity, on the other hand, takes place when the material undergoes phase transformation upon loading and unloading between martensite and austenite phases, which results in the ability to carry constant stresses for a long range of strains (Figure 2.1.1(b)). Specifically, in NiTi alloys which are the best known SMAs, phase transformation between the high temperature, i.e. austenite, and low

temperature, i.e. martensite, stable phases results in shape memory effect and pseudoelasticity. The solid state martensite-to-austenite or vice versa transformation are realized by twin formation and detwinning in the microstructure. In this part of the thesis the pseudoelasticity of NiTi alloys will be investigated from both microstructural and application perspectives.

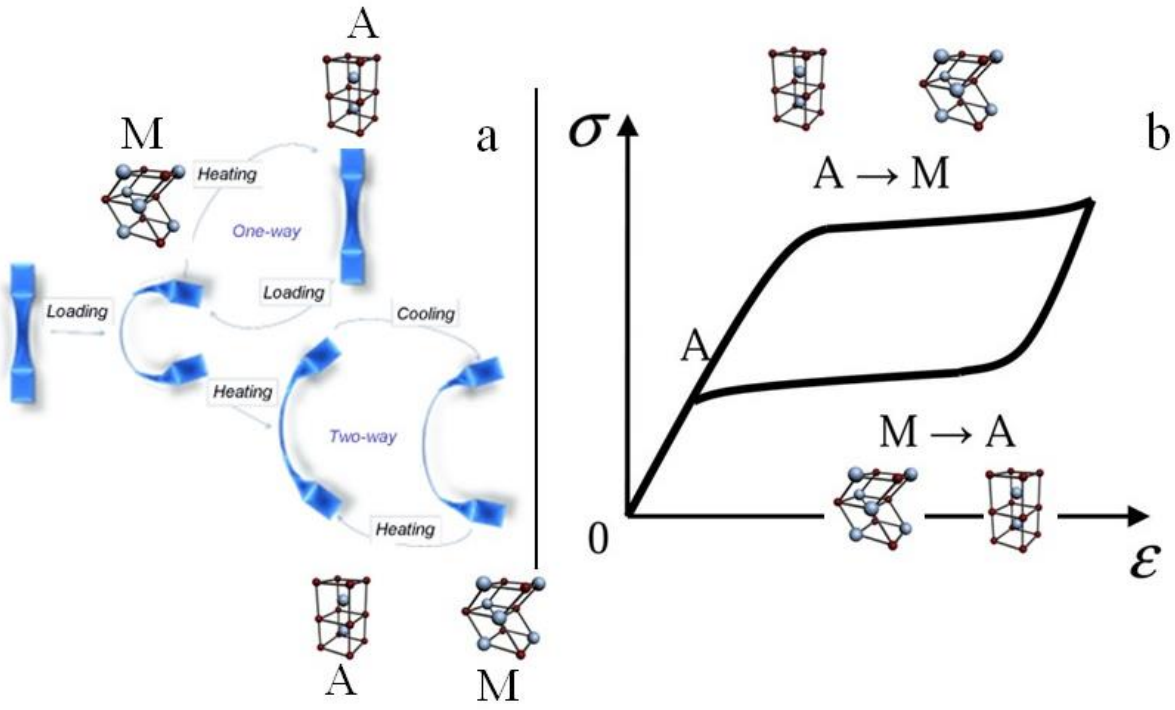

Figure 2.1.1: (a) One- and two-way shape memory effects [84] and **(b)** pseudoelasticity [85] ("A" and "M" stand for austenite, and martensite, respectively).

One of the major concerns regarding the utility of NiTi (SMAs) is their functional fatigue performance, where cyclic loading brings about deterioration of pseudoelasticity, shape memory effect, damping capacity, and significant changes in phase transformation temperatures [86]. Specifically, residual stresses and changes in the microstructure stemming from irreversible deformation induced by fatigue due to vacancy formation, grain boundary

sliding or dislocation motion alter the phase transformation capability, and thus, the shape memory characteristics of the alloy [87].

Numerous works have been undertaken addressing the fatigue problem in SMAs, which mostly focused on establishing fatigue lives for various strain amplitudes [88–96]. Part of these efforts were dedicated to the cyclic bending response of NiTi alloys, which is of significant importance in micro electro-mechanical systems and biomedical applications, where bending or twisting constitute the major loading modes. For instance, micro-pumps used in drug delivery, micro-grippers utilized in endoscopes and micro-sensors designed for detecting cancer are subject to bending loads at relatively high frequencies [97]. NiTi stents placed into femoral, coronary and carotid arteries, and the aorta constitute other examples to biomedical applications subject to complex cyclic loading, including bending stresses [98]. In order to ensure the reliability of NiTi SMAs under such conditions, functional properties, such as recoverable strain, pseudoelasticity and shape memory properties of NiTi SMAs were thoroughly investigated [96,99,100]. While many of these studies were restricted to the macroscopic scale, the works focusing on SMA thin films considered uniaxial tensile or compressive loading scenarios only [101–103]. However, despite the continuously increasing demand for the utility of SMAs in micro- and nano-scale applications, a thorough investigation of the cyclic bending response of at these small scales has not been undertaken yet, which constitutes one of the major motivations of the current work.

It has been demonstrated that a material's response at the nano- or micro-scale can deviate from that at the macroscopic scale, warranting a detailed investigation of the cyclic response of SMAs under bending prior to their utility in any of the aforementioned applications. To the best of the authors' knowledge, such an investigation is not available in the literature, however; evidence on the effect of scale difference on the material behavior has been demonstrated for other metallic materials. For instance, copper (Cu) thin films exhibited

a lower Young's modulus but higher yield and ultimate tensile strengths than their bulk counterparts under cyclic tensile loading. [104]. Similarly, persistent slip bands (PSBs) were prevalent in bulk Cu and gold (Au) samples upon deformation whereas they were absent in Cu and Au thin wires. Specifically, the existence of PSBs and the extrusions on these PSBs lead to local increases in the stress field, and thereby formation of several crack initiation sites [105]. Thus, their absence in the case of thin wires resulted in improved fatigue performance.

The aforementioned shape memory behavior and pseudoelasticity of NiTi alloys, on the other hand, have gained significant attention in medical field [98,106–108]. Among the wide of range of applications, the advantage of pseudoelastic behavior is taken in dentistry. In the case of orthodontic archwires, to illustrate, with the help of pseudoelasticity of NiTi alloys, constant stress application is made possible over large displacements which stands for large tooth displacements [98,106], which results in minimized tissue damage during treatment [109]. Moreover, the application of constant stress defeats expensive and troublesome readjustment procedures required for wires made of conventional materials in order to provide constant stress, such as medical grade stainless steel [106,110–113]. Hence, the pseudoelasticity of NiTi alloys, which is due to the austenite-to-martensite phase transformation above the austenite finish temperature and under straining out of the elastic range of the NiTi alloy, is very advantageous in medical field by leading to a state of constant stress [114].

As opposed to the significant pseudoelasticity which makes the utility possible in medicine, the biocompatibility of NiTi alloys is still subject to debate due to potential Ni release from the surface of the material. The release of Ni alloys to the human body may result in serious health problems, especially in Ni-allergic patients [115,116]. In the case of orthodontics, released Ni ions get directly into contact with the intraoral cavity which may cause complications, such as burning sensations and inflammation around or in the mouth,

and gingival hyperplasia [116]. Specifically, the major concern about the biocompatibility of NiTi alloys, i.e. Ni ion release, is dependent on the applied stress state, and the properties of both the sample surface and the body fluid (or tissue) the sample comes into contact with. For instance, it has been shown that Ni ion release is favored with increased acidity of the fluid and further plastic deformation due to applied stress [115,117]. In addition to the effects of the fluid and the stress state, the geometry of the sample has been forwarded to has a major contribution in the amount of ion released, where the surface finish and properties influences the amount of ion release together with the properties of fluid contacting the material [115]. In the case of applied stress on the material, Ni ion release behavior and biocompatibility experiments were carried out including both static [109,117] and cyclic [118,119] loads on NiTi samples.. However, the loading scheme in all these studies was selected as simple three-point bending, which does not simulate the actual stress state of orthodontic wires during dental treatments. The contribution through application of a more realistic loading condition is the possibility of exploration of ion release behavior especially when stress-assisted corrosion cracking (SCC) takes place. This phenomenon can be explained as the enhanced crack initiation with applied stress and resulting propagation of that initiated crack through the surface of the material in corrosive environments [118]. For NiTi alloys, the material is covered with a protective film which formed upon manufacturing. Therefore, when a stress is applied to the material, this protective film may fractured which results in the direct contact of the alloy with the corrosive environment causing Ni decomposition and release [120]. Moreover, the changes in the surface properties such as roughness and morphology due to chemical, thermal- or stress effects enhances crack initiation and/or propagation due to dissolution of the alloy [121–123].

Although several studies were conducted on the Ni ion release and corrosion behavior of NiTi archwires [109,115–119,123–128], an investigation on the Ni ion release due to SCC

and corresponding biocompatibility of the alloy which simulates both the chemical and mechanical conditions more realistically has not been forwarded yet. This study was carried out with the motivation to focus on this issue, such that experiments mimicking the actual intraoral conditions were designed and conducted on commercially available NiTi wires for orthodontic treatments.

2.1.2 Methods and Preliminary Work

In the current study, cyclic deformation response of micro-scale pseudoelastic nickel-titanium (NiTi) wires was investigated under bending. A thorough set of mechanical experiments and transmission electron microscopy (TEM) analyses were carried out in order to uncover the microstructural effects of the change from macroscopic to microscopic scale on the observed fatigue performance. The current findings constitute a step forward towards the utility of safe and reliable small-scale equipment benefiting from the pseudoelastic property of NiTi alloys.

In addition to investigation on fatigue response, a more application-based study were conducted on orthodontic NiTi wires. Aiming this objective, static immersion experiments in artificial saliva (AS) were carried out, such that the NiTi wires were subjected to AS for 31 days while attached to brackets fixated on upper dental arch mold model of an actual patient. Once experiments were completed, both the NiTi wires and the fluids in which these wires were immersed were deeply investigated to detect the changes in surface properties of the wires and chemical contents of the fluids due to ions released during experiments. The current set of findings demonstrates new structures deposited on the surface of the wires which are C- and Ca-rich corrosion products. Although these corrosion products were observed on both undeformed and bound archwires, the deposition behavior is altered between these two cases. Specifically, the stress concentration at the contact points of archwire with the brackets favors

SCC for the bound wire case, which results in micro-crack formation on the surface. These micro-cracks act as optimal nucleation sites for the corrosion product deposition. In addition, enhanced ion release is enhanced from these SCC regions on the surface of wire due to the high surface energy maintained at the cracked surfaces. Overall, the current study precisely indicated the requirement of laboratory experiments covering both the mechanical and chemical conditions of intraoral environment for a reliable investigation of biocompatibility of NiTi archwires.

2.2 MICRO-SCALE CYCLIC BENDING RESPONSE OF NiTi SHAPE MEMORY ALLOY

2.2.1 Materials and Methods

The micro-scale cyclic pseudoelastic response and the corresponding microstructure evolution of a NiTi alloy containing 50.7 at. % Ni was investigated. Geometrically uniform micro-scale samples were obtained by chemical etching of commercially available pseudoelastic NiTi wires with a diameter of 3.5 mm. The chemical etching was carried out in two stages, such that a solution with a $HF:HNO_3:H_2O$ ratio of 1:4:5 was utilized initially to quickly reduce the diameter to about 200 μm, followed by a slower rate of etching in $HF:HNO_3:H_2O$ with a ratio of 1:5:20 to ensure a uniform diameter along the longitudinal axis of each sample. In the current study, the diameter of the smallest geometrically homogenous wires was 35 μm (Figure 2.2.1, inset 1). The dashed line in the main figure represents the intermediate loading level, at which the hysteresis widths were compared, while the dashed line of inset 2 indicates the longitudinal axis of the undeformed wire. One end of the samples was clamped between two aluminum plates, and a commercial force sensor driven with 5 V DC supply was placed on an x-y-z-θ positioning stage to apply the load (Figure 2.2.1, inset 1). The effective length for each sample, *i.e.* the distance between the clamp and the point of loading was 8 mm. The sensor operates on the principle of differential capacitance measurement as a result of the motion of its shuttle [129]. Its output voltage and the specific sensor gain were multiplied to determine the magnitude of the applied force in Newton. Moreover, each step of loading and unloading was recorded by a camera connected to an optical microscope, such that the displacements measured in pixels could be converted to μm.

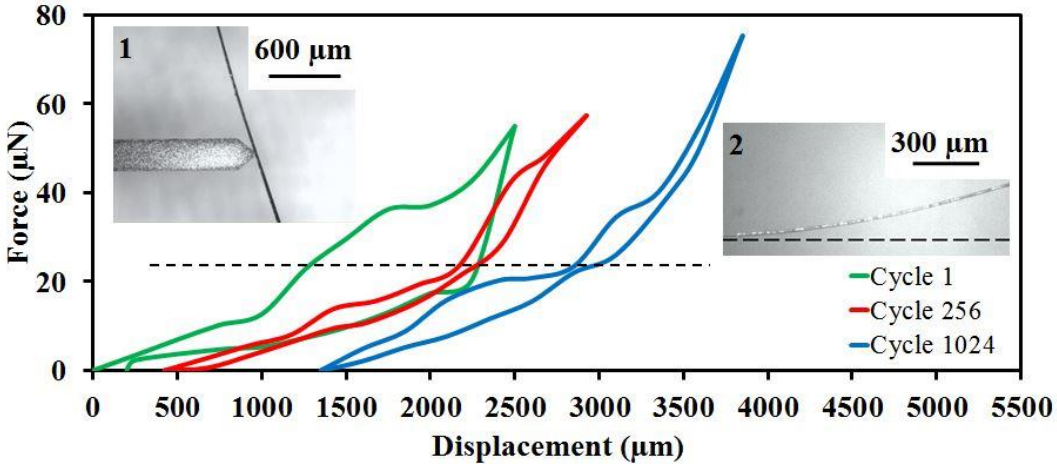

Figure 2.2.1: The pseudoelastic response of 35 μm NiTi wires under cyclic cantilever bending. Inset 1 and 2 show the sample under loading imposed by the force sensor, and the deformed sample following 1024 cycles, respectively.

2.2.2 Results and Discussion

Low-cycle fatigue experiments were carried out on 35 μm thick NiTi micro-wires with a maximum displacement of 2.5 mm (Figure 2.2.1), such that the applied strains could be restricted within a range large enough to observe the change in hysteresis and small enough to allow for gradual progress of plastic deformation under cyclic loading. Accordingly, the width of the stress–strain hysteresis decreases, the amount of irreversible strain increases, and the stress levels of the forward and reverse transformation plateaus decrease concomitant with the progressing cyclic loading. The corresponding hysteresis widths are depicted on Figure 2.2.1 for the intermediate loading level indicated by the dashed line. The values are nearly 1000 μm, 200 μm and 140 μm for the increasing order of number of cycles. One should note that the curves have irregular shapes, however; the same shapes were evident in all companion experiments, eliminating the possibility of scatter in data. Indeed, these observations agree well with the previous findings of work on CuAlNi pillars [130,131] and wires [132], and NiTi micro wires [133]. Specifically, consecutive compressive loading of the CuAlNi pillars

and wires led to the narrowing of hysteresis [130–132]. In the case of NiTi micro wires subjected to cyclic loading, both the hysteresis decreased and the irreversibility increased with progressing cyclic deformation [133]. In the current set of results, these effects are more apparent at earlier stages, and saturation is observed with increasing number of cycles, which is important in terms of the utility of cyclic deformation to stabilize pseudoelasticity [134].

These initial observations of the current study on the microscopic scale samples also stand in good agreement with the results of experiments conducted on macroscopic samples [134–136]. However, the decrease in the stress hysteresis is more pronounced for the current case when compared to macroscale results on similar materials [134–137]. Specifically, the narrowing of stress hysteresis was significant (about 30%) following 100 cycles of deformation in [321]-oriented macroscale NiTi single crystals, where the average precipitate size was 10 nm [136]. Despite the fact that the precipitate size is very close to 10 nm in the current material as well, the narrowing effect on hysteresis is even more substantial (about 80% after 256 cycles). Moreover, this lower narrowing of hysteresis was observed after cyclic investigations on macroscale polycrystalline NiTi samples, where pseudoelastic behavior still remained following 50 cycles [137], while the loading-unloading curves are almost overlapping each other after 256 cycles in this study. In addition to the difference in hysteresis behavior, the amount of residual strain after cyclic deformation is much lower at the microscale than it is in macroscale experiments [86,137].

It has been previously demonstrated that stress-induced martensite formation is associated with the phase transformation stresses, resulting in a decrease in stress levels with increasing number of fatigue cycles [80]. In the current experiments, the irreversible strain, which increased concomitant with the number of cycles, constitutes the evidence of plasticity associated with stress-induced martensite formation: following 1024 cycles, there is residual plastic strain which cannot be recovered by unloading the sample (Figure 2.2.1, inset 2).

Microstructural evolution of the samples was investigated with TEM. The TEM samples were extracted from locations as close as possible to the mid-plane of the wire. Interestingly, the selected area diffraction (SAD) pattern presented in Figure 2.2.2 demonstrates that the initial material had undergone a two-step B2→ R-phase→B19' austenite-to-martensite phase transformation prior to the experiments [138]. It is well known that precipitates play a key role in phase transformation since they constitute ideal nucleation sites for the B2→R-phase transformation [136,139]. It has been previously demonstrated that the R-phase nucleates at the Ni_4Ti_3 precipitates and grows into the matrix, whereas the B19' phase nucleates at the grain boundaries and propagates into the R-phase and grain interiors [139,140]. The B2→R-phase transformation elicits a narrow hysteresis and brings about superior functional fatigue resistance owing to the relatively small transformation strain of about 1% [141]. On the other hand, the R→B19' phase transformation exhibits a strain of the order of 10% [142]. This difference between the transformation strains stems from the corresponding difference in volume changes taking place during the B2→R→B19' and B2→B19' phase transformations [143].

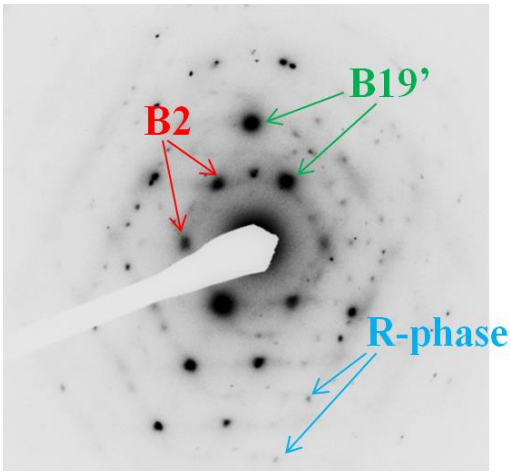

Figure 2.2.2 SAD pattern demonstrating the presence of three phases in the initial material: B2, R-phase and B19'.

The introduction of the R-phase leads to significant thermodynamical changes in the NiTi alloys [143]. Normally, the B19' phase is energetically more stable than the B2 phase below the temperature at which martensitic transformation starts. However, the B2→R-phase transition alters the thermodynamic balance of the system, such that the free energy of the R-phase becomes smaller than that of the B2 below the R-phase transition temperature, and depending on the amount of phase transformation, it may be smaller or larger than the free energy of the B19'. As a result, it is possible to have R-phase stabilized over B19', which results in different microstructure and mechanical response. In contrast to macro-scale samples, the B2→R-phase transformation is mostly suppressed in the micro-scale samples, and thus, only a small amount of stabilized R-phase was observed in the microstructure of the current samples.

It should also be noted that the R- and B2 phases possess different crystal structures: trigonal and cubic, respectively [140]. Consequently, the resulting stacking sequence of B19' phases are different upon R→B19' and B2→B19' transformations even though the product phase is the same [143]. Due to the very limited amount of B2→R-phase transformation in the current samples, the resulting B19' grains have almost the same stacking order in both cases.

From the microstructural point of view, there are two major outcomes regarding the precipitates and B19' grains. First of all, the current deformed material features precipitates that fall within two different size ranges: 3-12 nm and 30-50 nm (Figure 2.2.3), while the precipitate size of the undeformed material was 10-30 nm. This outcome contradicts the findings in the literature for an NiTi alloy processed at very similar conditions to those of the current study, such that an average precipitate size of 1 nm was evident [142]. This difference is attributed to the increase in the density of dislocations and twins during cyclic deformation, which significantly increases the number of nucleation sites for Ti_3Ni_4 precipitate formation

[138]. There is an absence of dislocations around smaller precipitates whereas dislocation accumulation was observed around larger ones, as previously reported in the literature [136]**.** This implies that the recoverability of the pseudoelastic strain during cyclic loading can be improved by restricting the size of the precipitates during the initial processing of the material. In Figure 2.2.3, larger precipitates with average grain size around 50 nm are visible. These larger precipitates are the major cause of irreversibility of the sample as they constitute stress concentration sites, promoting irreversible plastic deformation and high dislocation density. This influential effect of increasing average precipitate size on irreversibility is in good correspondence with recent findings on the cyclic deformation response of micro-scale NiTi wires [133]. In particular, the cyclic irreversibility increased with increasing average precipitate size, where this irreversible strain was attributed to dislocation slip imposed by cyclic deformation as evidenced by the absence of martensite in the fatigued microstructure [133].

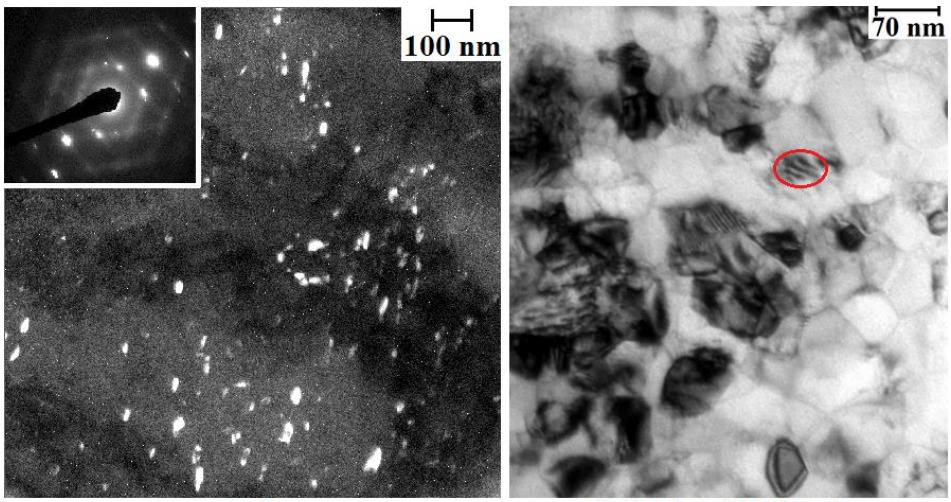

Figure 2.2.3 Dark-field TEM image showing the larger precipitates in the as-is material (left) and a bright-field TEM image demonstrating the presence of precipitates in the microstructure following 1024 cycles (right). The red circle represents the twinned variant of B19' with a grain size of ≈ 30 nm.

Another important observation is that a critical grain size was prevalent for B19' formation during deformation in the current material (Figure 2.2.3). The smallest B19' grain was about 30 nm in size, which is smaller than the 50 nm reported in literature [144]. This smaller critical grain size reveals that B19' nucleation is enhanced at the micro-scale. On the other hand, the amount of R-phase over the whole sample was calculated as less than 0.2 %, which supports the argument of enhanced B19' nucleation. A similar observation was reported for nano-scale NiTi pillars subjected to compression, where the R-phase was absent in the presence of demonstrated pseudoelasticity [145]. This implies that, as the diameter is reduced to the sub-micron level, the aforementioned effects of the R–phase would also be eliminated, such that the non–linearity of the pseudoelastic behavior is prevented, the elastic modulus becomes smaller, and temperature dependency can be lessened [141,146]. Moreover, reduction of the average grain size would also improve the homogeneity of the microstructure, and thus, the overall fatigue performance of the material.

Another point of discussion is the incomplete reverse transformation upon unloading evidenced by the presence of twinned martensite (Figure 2.2.4) and enlarged Ni_4Ti_3 (Figure 2.2.3) precipitates in the microstructure. Specifically, this irreversibility is associated with the restriction of the martensitic transformation, which is implied by an increase in the residual strain, leading to strain hardening with increasing number of cycles. Furthermore, the restricted martensitic transformation yields a significant reduction in transformation hysteresis (Figure 2.2.1). The underlying mechanism of hysteresis reduction with increased deformation is consistent with the previous observations on NiTi and NiTiCu [137]. Specifically, as cyclic deformation proceeded residual strains increased (Figure 2.2.1), hindering the transformation straining capability of the microstructure. This eventually leads to a decrease in the critical stress for martensitic transformation with ongoing cyclic deformation, which results in a narrower hysteresis (Figure 2.2.1).

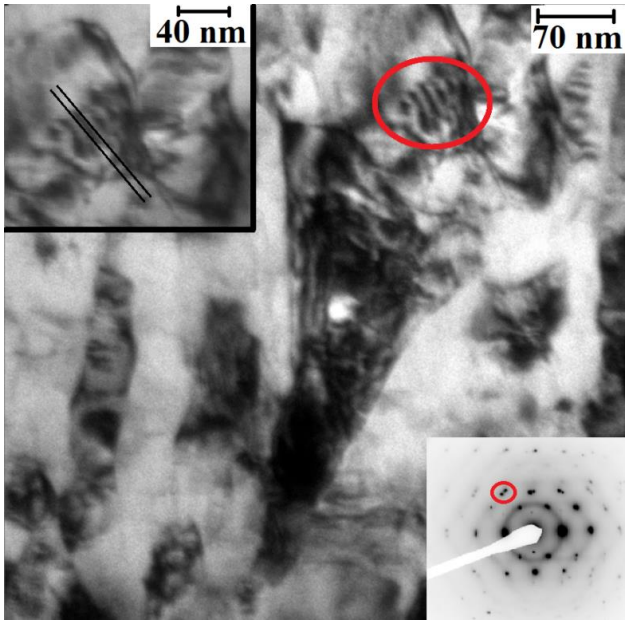

Figure 2.2.4 Bright-field TEM image showing the twinned variant of the B19’ phase marked by the red circle following 1024 cycles. The average distance between the twins (inset) is 10 nm.

2.2.3 Summary

Overall, the current findings clearly demonstrate that the cyclic bending response of the NiTi alloy leads to a scale-dependent microstructure evolution and pseudoelastic properties. Specifically, deformed samples exhibited significant irreversible strains, partially owing to the increased dislocation density observed around large precipitates. In addition, the change from the macroscopic to the microscopic scale has also been shown to favor the formation of B19’ over the stabilized R-phase. The bending fatigue experiments on NiTi wires at micro-scale have laid out the superior performance of these alloys. In the following section, an application-based study will be presented which is on the investigation of the biocompatibility of NiTi orthodontic archwires.

2.3 A CRITICAL APPROACH TO THE BIOCOMPATIBILITY TESTING OF NiTi ORTHODONTIC ARCHWIRES

2.3.1 Materials and Methods

Following the microstructural approach, a more application-based study was conducted on NiTi orthodontic wires. This work consists of static immersion experiments in AS to explore the changes in the surface properties of NiTi wires which are induced by SCC. Moreover, the possible ion release from orthodontic wires to intraoral cavity was investigated in these experiments. For these purposes, 18' slot 3M Unitek Gemini Roth metal brackets[2] were fixated to a dental mold model of the upper dental arch which were bonded with light cure adhesive (3M Unitek Transbond XT). The dental mold models were obtained from standard plastic upper jaw models for duplication, where alginate was used as impression material. Dental plaster was then cast into the alginate model and the obtained hard dental plaster was used as the dental mold.

The orthodontic archwires[3] made of NiTi were placed into the bracket slots with the following sequence: both bonding of the brackets and the binding procedure were performed from upper left second premolar to upper right second premolar. The NiTi archwire was bound conventionally with ligature wire. The archwire was inserted passively due to no crowding or rotations present on plaster models. Two sets of identical dental mold models were prepared with brackets attached onto them. However, on only one of them the NiTi archwires were attached in order to take the other for control measurements for post-experiment ion release measurements via Inductively Coupled Plasma-Mass Spectroscopy (ICP-MS) Dental molds both with and without archwires were immersed statically for 31 days

[2] 18' slot 3M Unitek Gemini Roth brackets and the corresponding metallic bases were manufactured from17-4PH and 304L stainless steels, respectively.
[3] 3M Unitek Smart Clip Nitinol heat activated archwires were used in the experiments.

in separate containers. The ingredients and the pH value of the AS employed in the current work are presented in Table 2.3.1. It should be noted that the pH of the natural saliva is about 7, however; a lower pH value (2.3) was preferred for AS in this study in order to include the effects of intraoral cavity consists possible dental plaque, and an aggressive environment that would potentially stem from nutritional habits, and the corresponding organic depositions and microorganisms which all results in decreased pH of the environment [113,115,147]. While preparing the AS, 1M of HCl was precisely added to the initial AS solution with pH value of near 7 until a level of acidity corresponding to a pH value of 2.3 was reached [126,127,147]. The prepared fluid in two beakers of 150 ml was initially observed to be stable and remained the same throughout the experiments confirming that there is no salt deposition. The immersed samples were kept in an electronically controlled water bath in order to keep them sustained at 37 °C, corresponding i.e. to the body temperature. Four sets of AS were used in the experiments: an as-prepared AS solution, AS with immersed undeformed wire in it, AS with only brackets attached to the mold, and AS with the wire attached onto the mold with brackets.

Table 2.3.1 Properties of the AS utilized in the current immersion experiments.

Ingredients	**Amount of Ingredients (g/l)**	**pH**
NaCl	0.4	2.3
KCl	0.4	
$CaCl_2 \cdot 2H_2O$	0.906	
$NaH_2PO_4 \cdot 2H_2O$	0.690	
$Na_2S \cdot 9H_2O$	0.005	
Urea	1	

After the 31-day-immersion-experiments, the undeformed and bound NiTi wires were examined using scanning electron microscopy (SEM) and Energy dispersive X-ray

spectroscopy (EDX) in order to observe SCC and the corresponding surface changes, as well as the new material deposition on the bracket-archwire contact regions. The SEM and EDX analyses were conducted on a Zeiss Ultra Plus field emission scanning electron microscope and compared to as-is archwire sample. The fluids in which the model and wire were immersed, moreover, were analyzed with a Perkin Elmer DRC II model ICP-MS to detect the any Ni or Ti ion release from the wire into the fluids. The observable mass interval was 2-270 amu and the observation limit was in the ng/L level.

2.3.2 Results and Discussion

SEM, EDX and optical microscopy analyses were comparatively utilized on wires after all three scenarios, i.e. as-is, undeformed and bound to model. The SEM images of these wires are given in Figures 2.3.1-2.3.4. In Figure 2.3.1, the surface of the as-is wire is shown which demonstrates homogeneity other than the processing marks and rare impurities. This homogeneity implies that any other structure or particle detected on undeformed and bound wire surface should be due to immersion in AS.

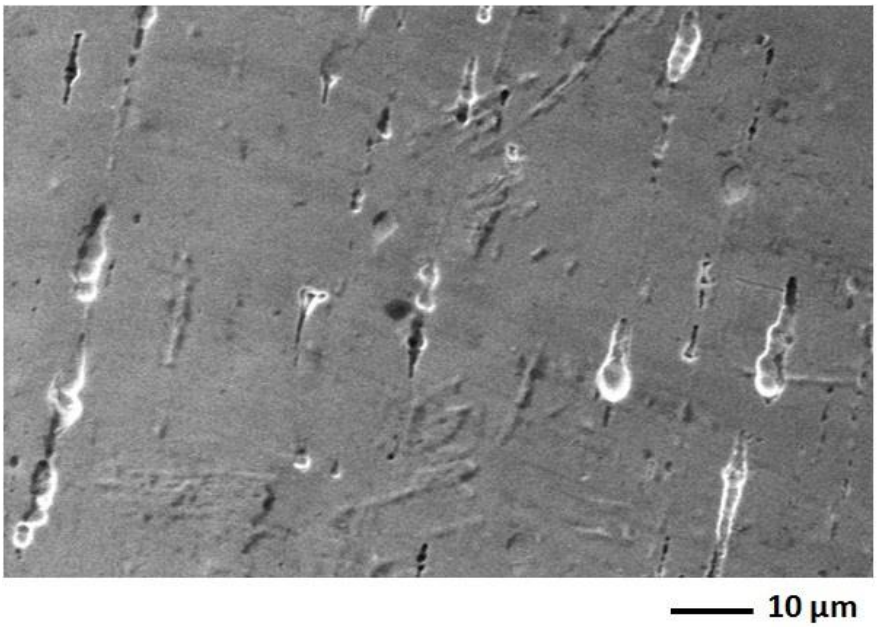

Figure 2.3.1 Representative SEM image of the as-is orthodontic archwire surface.

On the contrary to the smooth surface of the as-is wire, undeformed wire features darker areas spread randomly on the surface on the surface (Figure 2.3.2). Quantitative EDX analysis from these regions has shown that these areas mainly constitute C-rich structures (Table 2.3.2). Considering the high amount of C in prepared immersion fluid, i.e. AS and the previous works conducted on NiTi upon immersion in AS [113,115], the observed random C-rich structure deposition on the undeformed wire can be justified. The reason for random deposition is the uniformity of the wire without any singularities on the wire surface which will be the wire-bracket contact points for the bound wire case. Hence, without any singularities, the new structures were deposited around the impurities which were randomly distributed on the wire surface (Figure 2.3.1).

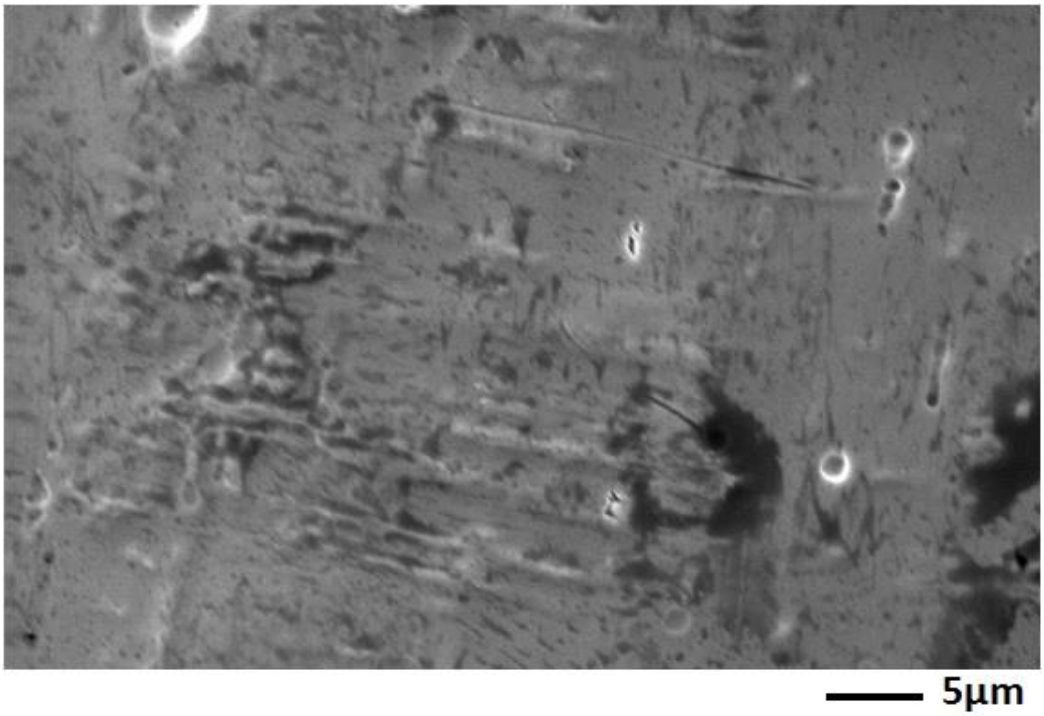

Figure 2.3.2 Representative SEM image of the undeformed orthodontic archwire surface immersed into AS.

Table 2.3.2 Relative quantities of the elements (provided in wt. %) detected on the new structures present on the undeformed archwire, new structures present on the bound archwire and the salt like structures present on the bound archwire immersed in AS for 31 days (Figure 2.3.2, 2.3.3 and 2.3.4) The "–" indicates that measured quantity of the regarding element was below the detection limit.

Element	Undeformed wire (new structures) wt.%	Bound wire (new structures) wt.%	Bound (salt-like structures wt.%
Carbon	16.50	14.72	4.59
Oxygen	9.37	10.30	26.92
Titanium	36.25	33.35	29.61
Nickel	37.88	33.19	28.27
Calcium	-	5.94	10.61
Phosphorus	-	2.50	-
Sum	100	100	100

Although there are same dark areas observed on the surface of bound wire as shown in Figure 2.3.3, they are rather concentrated at points between which there is a certain distance than being randomly distributed. Other than the localization of this new material deposition, the amount of it also increased (Figure 2.3.3) when compared to undeformed wire case (Figure 2.3.2). Similar to the ones on the surface of undeformed wire, the dark areas spotted on the surface of bound wire are composed of C-rich corrosion products as analyzed by quantitative EDX (Table 2.3.2). In addition to the dark C-rich areas there are white-colored salt-like material deposited on the bound wire (Figure 2.3.4) which were found to be Ca-rich after EDX analyses (Table 2.3.2). The Ca-rich material deposition is caused by the Ca release from the plaster model and is localized also similar to C-rich areas. The localization of new

materials deposited on the surface of bound wire required detailed observation via optical microscopy to detect whether this localization is present at a larger scale or not. In Figure 2.3.5, an integrated optical image of a section of wire surface is shown. Within this section of the wire, there are three distinctive points of localized corrosion product deposition.

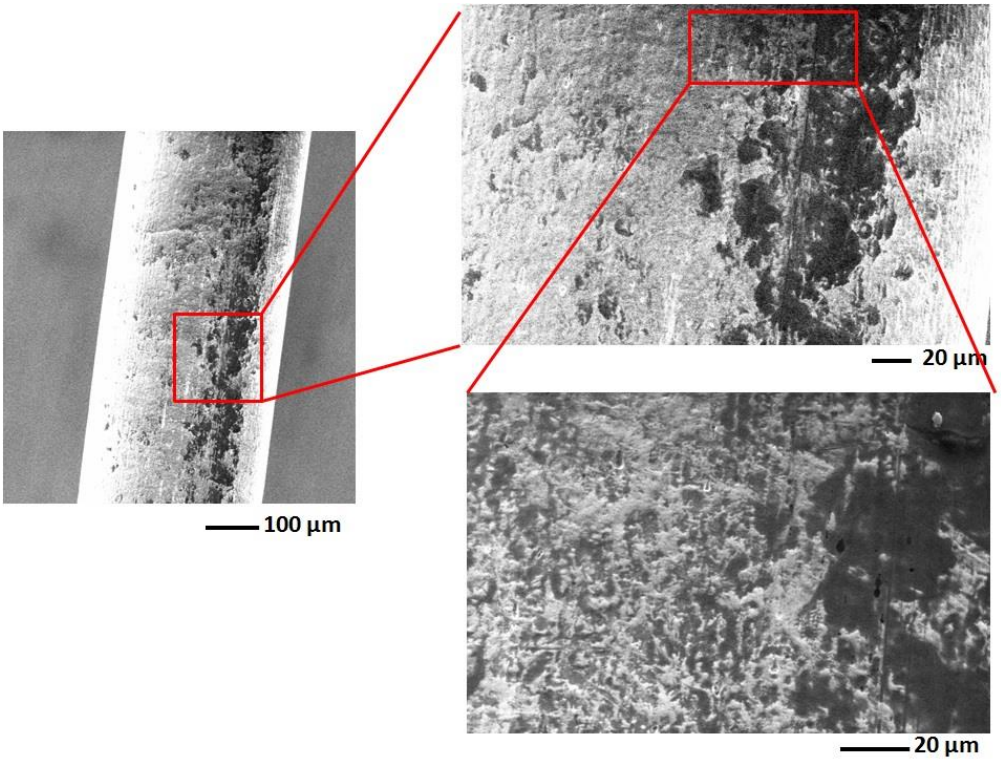

Figure 2.3.3 SEM images demonstrating C deposition on the bound orthodontic archwire immersed in AS.

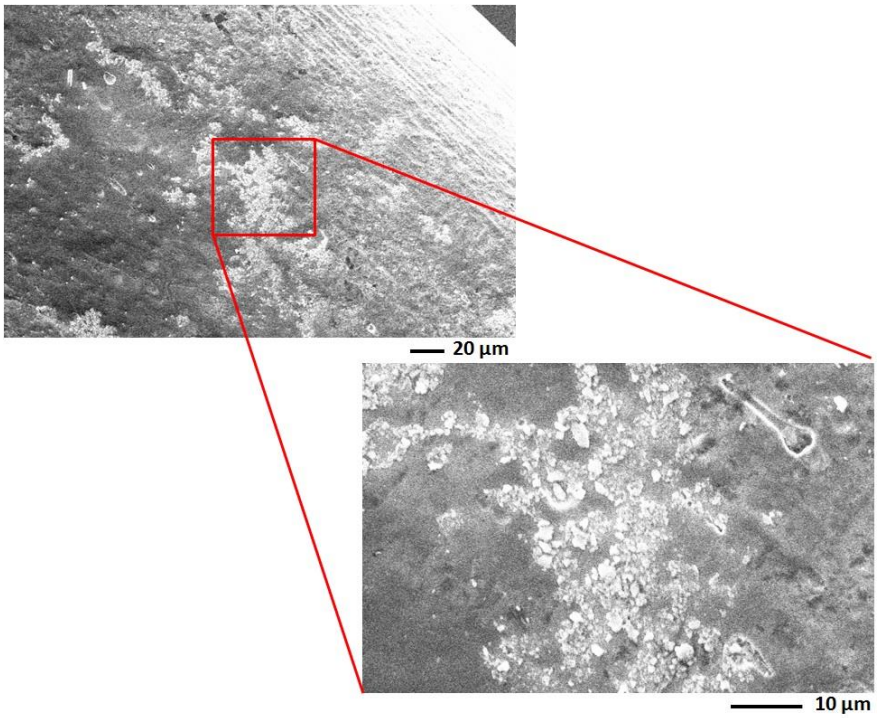

Figure 2.3.4 SEM images demonstrating Ca-rich phase deposition on the bound orthodontic archwire immersed in AS.

The near equally distant corrosion product deposition is evident from optical microscopy analyses where this distance between two repetitive deposition regions is about 1 cm (Figure 2.3.5). This distance is close to the distance between two repetitive teeth on the dental model proving that the wire-bracket contact points constitute ideal nucleation sites for corrosion products as they are higher energy regions due to stress concentration. This localization of corrosion products agree well with the previous study where the as-is wire immersed in AS compared to an orthodontic wire that was retrieved from a patient where there was a mechanical contact between the wire and brackets in intraoral cavity for the same time interval [113]. Similar to the current study, C-rich darker areas was observed on both the as-is and the retrieved wires, however; the depositions on the retrieved wires were localized at the contact points enough to be observed with the naked eye Adversely, there was no localization of corrosion product deposition which made the detection of it possible only under SEM for the immersed as-is wire case [113]. This localization was associated with the

easier nucleation at the wire-bracket contact points due to stress concentration [113]. A similar localization was reported in a previous work where in-service SCC took place causing the fracture of NiTi archwires [109]. The results indicated that the deposition of new materials composed of different elements such as Na, K, and Cl were localized around the tips of the cracks formed through SCC which are the stress concentration regions for that specific case [109].

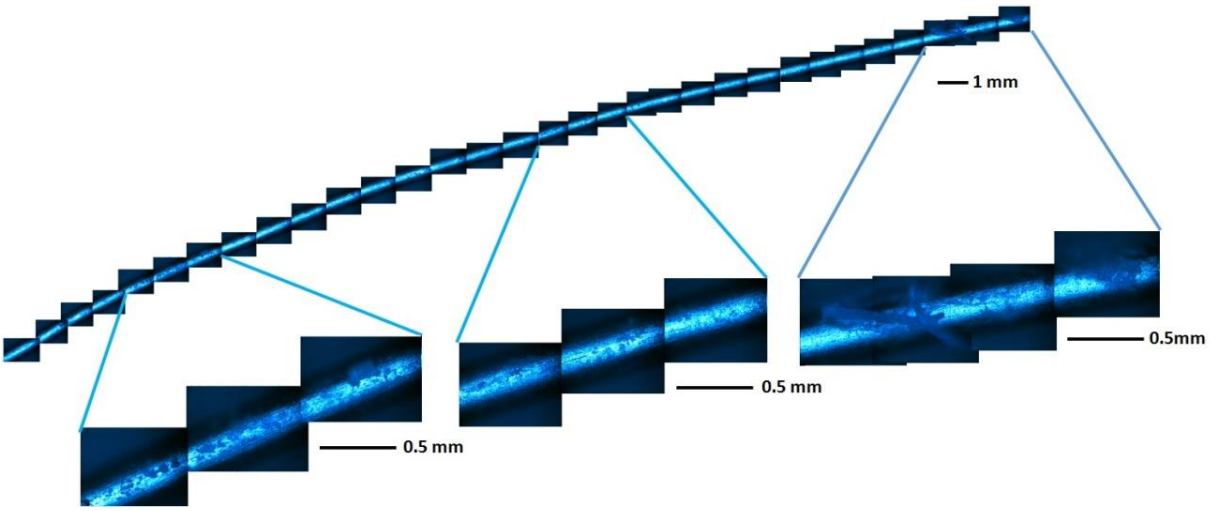

Figure 2.3.5 Optical microscope images of the bound orthodontic archwire immersed in AS Multiple high resolution images were gathered together to show the status of a meaningful segment of the wire upon being released from the mold.

The localized nucleation of new materials at critical regions featuring stress concentration such as impurities, grain boundaries and cracks have been investigated before of which the results revealed the higher energy attained at these regions enhances nucleation, hence, deposition of new materials since in that case the energy required for nucleation is lowered [148,149]. Therefore, the localized deposition of C- and Ca-rich corrosion products in the current study around wire-bracket contact points can be attributed to stress concentration present, thus higher energy attained, at these regions. In addition to stress concentration, Figure 2.3.6 demonstrates another significant reason for the localization of new material deposition, namely SCC. Specifically, in Figure 2.3.6(a) a crack formed on the

surface of wire is shown which formed via SCC since higher stresses are reached at the wire-bracket contact points and together with corrosive environment cracks can easily be initiated and propagates at these critical regions. The resulting crack, similar to other stress concentration regions, provide suitable places for nucleation which was also observed as there were corrosion products deposited around these cracks (Figure 2.3.6(b)). This localization along with the random deposition on undeformed wire surface proves that the wire-bracket sites are critical regions for SCC, and thus, they are more prone to corrosion product deposition. On the contrary to the localization observed with optical microscopy, it was not visible to the naked eye which was the case in the previous study where an orthodontic wire was retrieved from an actual patient [113]. The reason for fewer amounts of deposited materials at a higher magnification can be attributed to the lower amount and diversity of constituents present in AS than in the intraoral environment of the patient. The actual intraoral cavity of a patient includes nutrients in addition to saliva which reveals that eating habits may also affect the corrosion product deposition behavior.

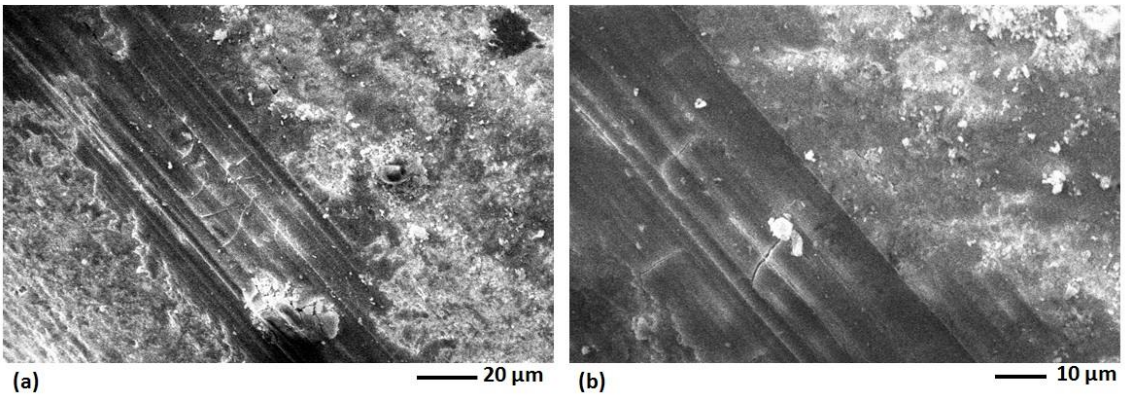

Figure 2.3.6 SEM images demonstrating (a) the crack formation due to SCC, and (b) the localization of the corrosion products near the cracks on the bound orthodontic archwire immersed in AS.

Post-immersion ICP-MS analyses were conducted in order to detect any ion release from the wire, brackets or model into the solution. In order to employ a comparative

approach, all three solutions with immersed undeformed wire, model and brackets, and bound wire to brackets bonded on model were examined. In addition to possible Ni or Ti ion release from the orthodontic wires, analyses were carried out such that any Ca or P ions may be released from dental model can be detected. The results of ICP-MS measurements are summarized in Table 2.3.3 for all scenarios. The reason that no result Ni or Ti in any of the solutions is that the measured values were below the detection limits for these ions which are 0.1 mg/L and 0.005 mg/L , respectively. As the most significant problem is Ni ion release in the case of NiTi alloys, it is crucial to justify this detection limit for the specific measurement with the critical limit for Ni intake (0.12-0.5mg/L) that can be harmful for the human body [128]. Since the detection limit, hence the released amount of Ni ion is almost equal to the lower critical limit, it is possible to argue that NiTi archwires utilized in the current work can be considered safe in terms of Ni-related health problems within the immersion period of 31 days. The safety resulting from low Ni ion release also indicated that although the wire-bracket sites enhances nucleation of corrosion products, they do not intensify Ni ion release since the cracks formed at these points are at microscale. Moreover, it can be proposed that since these microscale cracks are stress concentration points, mostly they are covered with corrosion products deposited as in Figure 2.3.6(b), which also prevents ion release from these cracks. The deposited layer of corrosion products resembles the protective film that covers the whole product initially. In addition to these, the reduced ion release due to deposited oxide layer on the surface of NiTi was forwarded where the possible ion release sites were stress-induced cracks [117].

Table 2.3.3 ICP-MS results demonstrating the Ni, Ti, Ca and P contents released into the AS solutions used in the experiments. The "–" indicates that measured ion concentration was below the detection limit.

AS solution	Ni	Ti	Ca (mg/L)	P (mg/L)
as-prepared AS	-	-	247±4	164±2
AS with undeformed wire	-	-	253±3	167±4
AS with brackets	-	-	623±11	-
AS with bound wire	-	-	658±10	-

On the contrary to Ni and Ti release below detection limits, Ca release was observed when the fluids with model compared to fluids without model (Table 2.3.3). Moreover, adversely, there was P release into fluids without model. These two findings together indicates that the Ca-rich precipitates on the bound wire surface were precipitates due to reaction between Ca and P ions present in AS solution. Furthermore, the presence of both Ca and P in as-prepared AS can be explained with the constituents of the solution (Table 2.3.1). Hence, the higher amount of Ca along with absence of P in the solution with bound wire is due to excessive amount of Ca ions released from the models, and, reaction between Ca and P present in the solution, respectively.

2.3.3 Summary

The biocompatibility of Nickel-Titanium (NiTi) wires utilized in orthodontics was investigated through *ex situ* immersion experiments which mimic chemical and mechanical conditions of intraoral cavity. The results demonstrated the importance of contact regions of wires and brackets since they constitute critical points, i.e. increased stress concentration, for new material deposition due to corrosion. These products inhibited a major Ni or Ti ion

release from the wires. In addition, wire-bracket contact makes a significant difference from the experiments where the mechanical contact is absent when the results are compared, such that the former set of experiments successfully simulated the actual intraoral cavity in terms of formation and localization of new material deposition at the contact sites. Consequently, the current study indicates that the association of chemical and mechanical conditions of the actual intraoral environment is crucial for a more correct biocompatibility experiment.

2.4 CONCLUSION AND FUTURE WORK

A thorough TEM-based study was carried out on the microstructural response of pseudoelastic NiTi alloy. Cyclic-bending tests were conducted on a micro-scale wire of which the diameter was 35 μm. The results revealed that changing from macro- to micro-scale resulted in narrower hysteresis and decreased irreversibility with an increase in the number of cycles. In addition to hysteresis behavior, the size of precipitations formed within the microstructure has shown to be increased upon going down to microscale as a result of increased dislocation density which induces extra nucleation sites for intermediate precipitates in NiTi alloy. Overall, the pseudoelastic properties of NiTi at microscale were shown to be superior to that at the macro-scale, implying a better performance at lower scale.

Following the micro-scale cyclic response of NiTi alloys, an application-based study was carried out on NiTi archwires. In order to examine the effect of mechanical contact in intraoral environment, wires were bound to brackets which were fixated on a plaster dental model. The static immersion experiments in artificial saliva were conducted for 31 days. After immersion period, both wires and solutions were analyzed via scanning electron microscopy and inductively coupled plasma-mass spectroscopy, respectively. The results demonstrated the localized deposition of corrosion products around the wire-bracket contacts due to higher surface energy of these regions. In addition, SCC observed to occur at the contact sites, related to the higher stress concentration. On the other hand, no Ni release was detected above critical limits which was attributed to the blocking of micro-scale cracks at the contact regions with deposited corrosion products.

As the future work of this part of the thesis, NiTi wires of decreased diameter than the commercially available ones can be utilized in biocompatibility investigation. This might not only make the examination of ion release at microscale possible but can also demonstrate the superiority of lowered scale wires in orthodontic applications.

REFERENCES

[1] D. Canadinc, PhD Thesis, University of Illinois at Urbana-Champaign, USA, 2005.

[2] B.K. Zuidema, D.K. Subramanyam, W.C. Leslie, Metall. Trans. A 18 (1987) 1629.

[3] P.H. Adler, G.B. Olson, W.S. Owen, Metall. Trans. A 17 (1986) 1725.

[4] D. Canadinc, H. Sehitoglu, H.J. Maier, Y.I. Chumlyakov, Acta Mater. 53 (2005) 1831.

[5] D. Canadinc, H. Sehitoglu, H.J. Maier, D. Niklasch, Y.I. Chumlyakov, Int. J. Solids Struct. 44 (2007) 34.

[6] Y.N. Dastur, W.C. Leslie, Metall. Trans. A 12 (1981) 749.

[7] I. Karaman, H. Sehitoglu, Y.I. Chumlyakov, H.J. Maier, I. V Kireeva, Metall. Mater. Trans. A 32 (2001) 695.

[8] I. Karaman, H. Sehitoglu, A.J. Beaudoin, Y.I. Chumlyakov, H.J. Maier, C.N. Tome, Acta Mater. 48 (2000) 2031.

[9] I. Karaman, H. Sehitoglu, Y.I. Chumlyakov, H.J. Maier, I. Kireeva, Scr. Mater. 44 (2001) 337.

[10] I. Karaman, H. Sehitoglu, K. Gall, Y.I. Chumlyakov, H.J. Maier, Acta Mater. 48 (2000) 1345.

[11] S. Curtze, V.-T. Kuokkala, Acta Mater. 58 (2010) 5129.

[12] O. Bouaziz, S. Allain, C.P. Scott, P. Cugy, D. Barbier, Curr. Opin. Solid State Mater. Sci. 15 (2011) 141.

[13] J.-E. Jin, Y.-K. Lee, Acta Mater. 60 (2012) 1680.

[14] A. Dumay, J.-P. Chateau, S. Allain, S. Migot, O. Bouaziz, Mater. Sci. Eng. A 483-84 (2008) 184.

[15] S. Allain, J.P. Chateau, O. Bouaziz, S. Migot, N. Guelton, Mater. Sci. Eng. A 387 (2004) 158.

[16] Y.F.F. Shen, C.H.H. Qiu, L. Wang, X. Sun, X.M.M. Zhao, L. Zuo, Mater. Sci. Eng. A 561 (2013) 329.

[17] I. Gutierrez-Urrutia, D. Raabe, Acta Mater. 59 (2011) 6449.

[18] K. Renard, S. Ryelandt, P.J. Jacques, Mater. Sci. Eng. A 527 (2010) 2969.

[19] O. Bouaziz, H. Zurob, B. Chehab, J.D. Embury, S. Allain, M. Huang, Mater. Sci. Technol. 27 (2011) 707.

[20] W.S. Owen, M. Grujicic, Acta Mater. 47 (1999) 111.

[21] Y. Chumlyakov, I. Kireeva, E. Zakharova, N. Luzginova, H. Sehitoglu, I. Karaman, Russ. Phys. J. 45 (2002) 274.

[22] S. Lee, J. Kim, S.-J. Lee, B.C. De Cooman, Scr. Mater. 65 (2011) 528.

[23] O. Grassel, L. Kruger, G. Frommeyer, L.W. Meyer, Int. J. Plast. 16 (2000) 1391.

[24] J.D. Yoo, S.W. Hwang, K.-T. Park, Mater. Sci. Eng. A 508 (2009) 234.

[25] R. Ueji, N. Tsuchida, D. Terada, N. Tsuji, Y. Tanaka, A. Takemura, K. Kunishige, Scr. Mater. 59 (2008) 963.

[26] S. Allain, J.-P. Chateau, D. Dahmoun, O. Bouaziz, Mater. Sci. Eng. A 387-389 (2004) 272.

[27] E. Bayraktar, F.A. Khalid, C. Levaillant, J. Mater. Process. Technol. 147 (2004) 145.

[28] D. Barbier, V. Favier, B. Bolle, Mater. Sci. Eng. A 540 (2012) 212.

[29] E.G. Astafurova, M.S. Tukeeva, G.G. Zakharova, E.V. Melnikov, H.J. Maier, Mater. Charact. 62 (2011) 588.

[30] M. Jabłońska, A. Śmiglewicz, Defect Diffus. Forum 334-335 (2013) 177.

[31] K. Renard, P.J. Jacques, Mater. Sci. Eng. A 542 (2012) 8.

[32] K. Renard, H. Idrissi, D. Schryvers, P.J. Jacques, Steel Res. Int. 83 (2012) 385.

[33] K. Jeong, J.-E. Jin, Y.-S. Jung, S. Kang, Y.-K. Lee, Acta Mater. 61 (2013) 3399.

[34] D. Barbier, N. Gey, S. Allain, N. Bozzolo, M. Humbert, Mater. Sci. Eng. A 500 (2009) 196.

[35] R. Ueji, Y. Takagi, N. Tsuchida, K. Shinagawa, Y. Tanaka, T. Mizuguchi, Mater. Sci. Eng. A 576 (2013) 14.

[36] S.M. Toker, D. Canadinc, A. Taube, G. Gerstein, H.J. Maier, Mater. Sci. Eng. A 593 (2014) 120.

[37] H. Idrissi, K. Renard, L. Ryelandt, D. Schryvers, P.J. Jacques, Acta Mater. 58 (2010) 2464.

[38] O. Bouaziz, S. Allain, C. Scott, Scr. Mater. 58 (2008) 484.

[39] P. Guo, L. Qian, J. Meng, F. Zhang, L. Li, Mater. Sci. Eng. A 584 (2013) 133.

[40] J.S. Jeong, W. Woo, K.H. Oh, S.K. Kwon, Y.M. Koo, Acta Mater. 60 (2012) 2290.

[41] H.-G. Lambers, C.J. Rüsing, T. Niendorf, D. Geissler, J. Freudenberger, H.J. Maier, Int. J. Fatigue 40 (2012) 51.

[42] S.-J. Lee, J. Kim, S.N. Kane, B.C. De Cooman, Acta Mater. 59 (2011) 6809.

[43] Y. Li, L. Zhu, Y. Liu, Y. Wei, Y. Wu, D. Tang, Z. Mi, J. Mech. Phys. Solids 61 (2013) 2588.

[44] T. Niendorf, C.J. Rüsing, A. Frehn, Y.I. Chumlyakov, H.J. Maier, Scr. Mater. 67 (2012) 875.

[45] A. Saeed-Akbari, L. Mosecker, A. Schwedt, W. Bleck, Metall. Mater. Trans. A 43 (2011) 1688.

[46] T.S. Wang, R.J. Hou, B. Lv, M. Zhang, F.C. Zhang, Mater. Sci. Eng. A 465 (2007) 68.

[47] S. Xu, D. Ruan, J.H. Beynon, Y. Rong, Mater. Sci. Eng. A 573 (2013) 132.

[48] J. Gil Sevillano, F. de las Cuevas, Scr. Mater. 66 (2012) 978.

[49] A. Khosravifard, M.M. Moshksar, R. Ebrahimi, Mater. Des. 52 (2013) 495.

[50] R. Ueji, K. Harada, N. Tsuchida, K. Kunishige, Mater. Sci. Forum 561-565 (2007) 107.

[51] D.R. Steinmetz, T. Jäpel, B. Wietbrock, P. Eisenlohr, I. Gutierrez-Urrutia, A. Saeed-Akbari, T. Hickel, F. Roters, D. Raabe, Acta Mater. 61 (2013) 494.

[52] I.B. Timokhina, A. Medvedev, R. Lapovok, Mater. Sci. Eng. A 593 (2014) 163.

[53] A.S. Hamada, L.P. Karjalainen, J. Puustinen, Mater. Sci. Eng. A 517 (2009) 68.

[54] D. Li, Y. Wei, C. Liu, L. Hou, D. Liu, X. Jin, J. Iron Steel Res. Int. 17 (2010) 67.

[55] I. Karaman, H. Sehitoglu, K. Gall, Y.I. Chumlyakov, Scr. Mater. 38 (1998) 1009.

[56] B. Hutchinson, N. Ridley, Scr. Mater. 55 (2006) 299.

[57] C. Efstathiou, H. Sehitoglu, Acta Mater. 58 (2010) 1479.

[58] L. Qian, X. Feng, F. Zhang, Mater. Trans. 52 (2011) 1623.

[59] F.C. Liu, Z.N. Yang, C.L. Zheng, F.C. Zhang, Scr. Mater. 66 (2012) 431.

[60] C. Iglesias, G. Solórzano, B. Schulz, Mater. Charact. 60 (2009) 971.

[61] E.G. Astafurova, Y.I. Chumlyakov, H.J. Maier, Int. J. Fract. 160 (2009) 143.

[62] D. Canadinc, C. Efstathiou, H. Sehitoglu, Scr. Mater. 59 (2008) 1103.

[63] D. Canadinc, I. Karaman, H. Sehitoglu, Y.I. Chumlyakov, H.J. Maier, Metall. Mater. Trans. A 34 (2003) 1821.

[64] P. Franciosi, F. Tranchant, J. Vergnol, Acta Metall. Mater. 41 (1993) 1543.

[65] G. Frommeyer, U. Brüx, P. Neumann, ISIJ Int. 43 (2003) 438.

[66] G.J.L. van der Wegen, P.M. Bronsveld, J.T.M. de Hosson, Scr. Metall. 14 (1980) 285.

[67] A.S. Hamada, L.P. Karjalainen, M.C. Somani, Mater. Sci. Eng. A 467 (2007) 114.

[68] T. Shun, C.M. Wan, J.G. Byrne, Acta Metall. Mater. 40 (1992) 3407.

[69] O. Onal, C. Ozmenci, D. Canadinc, Front. Mater. 1 (2014) 16.

[70] M.S. Matoso, R.B. Figueiredo, M. Kawasaki, D.B. Santos, T.G. Langdon, Scr. Mater. 67 (2012) 649.

[71] R.E. Schramm, R.P. Reed, Metall. Trans. A 6 (1975) 1345.

[72] S. Plimpton, J. Comput. Phys. 117 (1995) 1.

[73] M.I. Mendelev, a. H. King, Philos. Mag. (2012) 1.

[74] G.J. Ackland, D.J. Bacon, a. F. Calder, T. Harry, Philos. Mag. A 75 (1997) 713.

[75] B. Bal, B. Gumus, G. Gerstein, D. Canadinc, H.J. Maier, Mater. Sci. Eng. A 632 (2015) 29.

[76] N. Li, Y.D. Wang, R. Lin Peng, X. Sun, P.K. Liaw, G.L. Wu, L. Wang, H.N. Cai, Acta Mater. 59 (2011) 6369.

[77] T. Niendorf, C. Lotze, D. Canadinc, A. Frehn, H.J. Maier, Mater. Sci. Eng. A 499 (2009) 518.

[78] W.-S. Lee, T.-H. Chen, Proc. Inst. Mech. Eng. Part C J. Mech. Eng. Sci. 216 (2002) 971.

[79] M. Hokka, V.-T. Kuokkala, S. Curtze, T. Vuoristo, M. Apostol, J. Phys. IV 134 (2006) 1301.

[80] X. Wang, B. Xu, Z. Yue, J. Alloys Compd. 463 (2008) 417.

[81] S. Miyazaki, K. Otsuka, 17 (1986) 53.

[82] G. Mogylnyy, I. Glavatskyy, N. Glavatska, O. Söderberg, Y. Ge, V.K. Lindroos, Scr. Mater. 48 (2003) 1427.

[83] N. Nakanishi, T. Mori, S. Miura, Y. Murakami, S. Kachi, Philos. Mag. 28 (1973) 277.

[84] J.M. Raquez, S. Vanderstappen, F. Meyer, P. Verge, M. Alexandre, J.M. Thomassin, C. Jérôme, P. Dubois, Chem. - A Eur. J. 17 (2011) 10135.

[85] Q. Pan, C. Cho, Sensors 7 (2007) 1887.

[86] G. Eggeler, E. Hornbogen, A. Yawny, A. Heckmann, M. Wagner, Mater. Sci. Eng. A 378 (2004) 24.

[87] P. Krulevitch, A.P. Lee, P.B. Ramsey, J.C. Trevino, J. Hamilton, M.N. Allen, J. Microelectromechanical Syst. 5 (1996) 270.

[88] M. Dolce, D. Cardone, Int. J. Mech. Sci. 47 (2005) 1693.

[89] S. Miyazaki, K. Mizukoshi, T. Ueki, T. Sakuma, Y. Liu, Mater. Sci. Eng. A 273-275 (1999) 658.

[90] X.J. Yan, D.Z. Yang, M. Qi, Mater. Charact. 57 (2006) 58.

[91] A. Figueiredo, P. Modenesi, V. Buono, Int. J. Fatigue 31 (2009) 751.

[92] T. Sawaguchi, G. Kausträter, A. Yawny, M. Wagner, G. Eggeler, Metall. Mater. Trans. A 34 (2003) 2847.

[93] J. Zurbitu, R. Santamarta, C. Picornell, W.M. Gan, H.-G. Brokmeier, J. Aurrekoetxea, Mater. Sci. Eng. A 528 (2010) 764.

[94] S. Bernard, V.K. Balla, S. Bose, A. Bandyopadhyay, Mater. Sci. Eng. C 31 (2011) 815.

[95] Y. Kim, Mater. Trans. 43 (2002) 1703.

[96] J. Rejzner, C. Lexcellent, B. Raniecki, Int. J. Mech. Sci. 44 (2002) 665.

[97] Y. Fu, H. Du, W. Huang, S. Zhang, M. Hu, Sensors Actuators A Phys. 112 (2004) 395.

[98] T. Duerig, A. Pelton, D. Sto, Mater. Sci. Eng. A 275 (1999) 149.

[99] V.S. Afonina, R.M. Gizatullin, D. V. Gunderov, V.S. Kalashnikov, V. V. Koledov, V.G. Shavrov, V. V. Istomin-Kastrovsky, ESOMAT 2009 - 8th Eur. Symp. Martensitic Transform. 06015 (2009) 1.

[100] M. Abedini, H.M. Ghasemi, M. Nili Ahmadabadi, Mater. Des. 30 (2009) 4493.

[101] K. Tanaka, T. Hayashi, Y. Itoh, H. Tobushi, Mech. Mater. 13 (1992) 207.

[102] K. Tanaka, Res Mech. 18 (1986) 251.

[103] F.D. Fischer, M. Berveiller, K. Tanaka, E.R. Oberaigner, Arch. Appl. Mech. 64 (1994) 54.

[104] D.T. Read, Int. J. Fatigue 20 (1998) 203.

[105] R. Hofbeck, K. Hausmann, B. Ilschner, H.U. Künzi, Scr. Metall. 20 (1986) 1601.

[106] R.J. Nikolai, Semin. Orthod. 3 (1997) 157.

[107] G. Mani, M.D. Feldman, D. Patel, C.M. Agrawal, Biomaterials 28 (2007) 1689.

[108] A. Bansiddhi, T.D. Sargeant, S.I. Stupp, D.C. Dunand, Acta Biomater. 4 (2008) 773.

[109] J. Wang, N. Li, G. Rao, E.-H. Han, W. Ke, Dent. Mater. 23 (2007) 133.

[110] Z. Davidovitch, V. Krishnan, Am. J. Orthod. Dentofacial Orthop. 135 (2009) 222.

[111] H. Wehrbein, P. Göllner, J. Orofac. Orthop. 68 (2007) 443.

[112] A. Van Schepdael, J. Vander Sloten, L. Geris, J. Biomech. 46 (2013) 470.

[113] S.M. Toker, D. Canadinc, Mater. Sci. Eng. C 40 (2014) 142.

[114] S. Miyazaki, K. Otsuka, ISIJ Int. 29 (1989) 353.

[115] S.M. Toker, D. Canadinc, H.J. Maier, O. Birer, Mater. Sci. Eng. C. Mater. Biol. Appl. 36 (2014) 118.

[116] K. House, F. Sernetz, D. Dymock, J.R. Sandy, A.J. Ireland, Am. J. Orthod. Dentofacial Orthop. 133 (2008) 584.

[117] J.-K. Liu, T.-M. Lee, I.-H. Liu, Am. J. Orthod. Dentofacial Orthop. 140 (2011) 166.

[118] O. Prymak, A. Klocke, B. Kahl-Nieke, M. Epple, Mater. Sci. Eng. A 378 (2004) 110.

[119] A. Milheiro, C. Kleverlaan, J. Muris, A. Feilzer, P. Pallav, Dent. Mater. 28 (2012) 548.

[120] E.M. Al-Waheidi, Quintessence Int. (Berl). 26 (1995) 385.

[121] M.R. Grimsdottir, A. Hensten-Petterseri, Dent. Mater. 13 (1997) 163.

[122] H.-H. Huang, Dent. Mater. 23 (2007) 24.

[123] D.K. Pun, D.W. Berzins, Dent. Mater. 24 (2008) 221.

[124] C. Heßing, J. Frenzel, M. Pohl, S. Shabalovskaya, Mater. Sci. Eng. A 486 (2008) 461.

[125] O. Mockers, D. Deroze, J. Camps, Dent. Mater. 18 (2002) 311.

[126] T.-H. Lee, C.-C. Wang, T.-K. Huang, L.-K. Chen, M.-Y. Chou, H.-H. Huang, J. Alloys Compd. 488 (2009) 482.

[127] X. Li, J. Wang, E. Han, W. Ke, Acta Biomater. 3 (2007) 807.

[128] H.-H. Huang, Y.-H. Chiu, T.-H. Lee, S.-C. Wu, H.-W. Yang, K.-H. Su, C.-C. Hsu, Biomaterials 24 (2003) 3585.

[129] D. Zhang, J. Breguet, R. Clavel, V. Sivakov, S. Christiansen, J. Michler, J. Microelectromechanical Syst. 19 (2010) 663.

[130] Y. Chen, X. Zhang, D.C. Dunand, C.A. Schuh, Appl. Phys. Lett. 95 (2009) 171906.

[131] J. San Juan, M.L. Nó, C.A. Schuh, Adv. Mater. 20 (2008) 272.

[132] J. San Juan, M.L. Nó, C.A. Schuh, J. Mater. Res. 26 (2011) 2461.

[133] R. Delville, B. Malard, J. Pilch, P. Sittner, D. Schryvers, Int. J. Plast. 27 (2011) 282.

[134] S. Miyazaki, T. Imai, Y. Igo, K. Otsuka, E. Procedure, Metall. Trans. A 17 (1986) 115.

[135] Y. Liu, I. Houver, H. Xiang, L. Bataillard, S. Miyazaki, Metall. Mater. Trans. A 30 (1999) 1275.

[136] K. Gall, H.J. Maier, Acta Mater. 50 (2002) 4643.

[137] B. Strnadel, S. Ohashi, H. Ohtsuka, T. Ishihara, S. Miyazaki, Mater. Sci. Eng. A 202 (1995) 148.

[138] M.F.-X. Wagner, S.R. Dey, H. Gugel, J. Frenzel, C. Somsen, G. Eggeler, Intermetallics 18 (2010) 1172.

[139] A. Dlouhý, O. Bojda, C. Somsen, G. Eggeler, Mater. Sci. Eng. A 481-482 (2008) 409.

[140] J. Michutta, C. Somsen, A. Yawny, A. Dlouhy, G. Eggeler, Acta Mater. 54 (2006) 3525.

[141] P. Šittner, M. Landa, P. Lukáš, V. Novák, Mech. Mater. 38 (2006) 475.

[142] C.P. Frick, A.M. Ortega, J. Tyber, A.E.M.E.M. Maksound, H.J. Maier, Y. Liu, K. Gall, Mater. Sci. Eng. A 405 (2005) 34.

[143] H.C. Ling, R.O.Y. Kaplow, Metall. Trans. A 51 (1981) 193.

[144] T. Waitz, T. Antretter, F.D. Fischer, N.K. Simha, H.P. Karnthaler, J. Mech. Phys. Solids 55 (2007) 419.

[145] J. Ye, R.K. Mishra, A.R. Pelton, A.M. Minor, Acta Mater. 58 (2010) 490.

[146] S. Miyazaki, K. Otsuka, Philos. Mag. A 50 (1984) 393.

[147] R.R. Al-Hity, H.F. Kappert, S. Viennot, F. Dalard, B. Grosgogeat, Dent. Mater. 23 (2007) 679.

[148] R. Huang, Y. Han, Mater. Sci. Eng. C. Mater. Biol. Appl. 33 (2013) 2353.

[149] Y. Estrin, E.P. Ivanova, A. Michalska, V.K. Truong, R. Lapovok, R. Boyd, Acta Biomater. 7 (2011) 900.